Editors' Suggestion

Microscopic calculation of fission product yields for odd-mass nuclei

N. Schunck [1,*] M. Verriere [1] G. Potel Aguilar,[1] R. C. Malone [1] J. A. Silano [1]
A. P. D. Ramirez [1] and A. P. Tonchev [1,2]

[1]*Nuclear and Chemical Sciences Division, Lawrence Livermore National Laboratory, Livermore, California 94551, USA*
[2]*Department of Physics, Duke University, Durham, North Carolina 27708-0308, USA*

Fission data are essential inputs to reaction networks involved in nucleosynthesis simulations and nuclear forensics. In such applications as well as in the description of multichance fission, the characteristics of fission for odd-mass nuclei are just as important as those for even-even nuclei. The fission theories that aim at explicitly describing fission dynamics are typically based on some variant of the nuclear mean-field theory. In such cases, the treatment of systems with an odd number of particles is markedly more involved, both formally and computationally. In this article, we use the blocking prescription of the Hartree-Fock-Bogoliubov theory with Skyrme energy functionals to compute the deformation properties of odd-mass uranium isotopes. We show that the resulting fission fragment distributions depend quite significantly on the spin of the odd neutron. By direct calculation of the spin distribution of the fissioning nucleus, we propose a methodology to rigorously predict the charge and mass distributions in odd-mass nuclei.

I. INTRODUCTION

The theory of nuclear fission has a long and rich history [1] and yet, it is still undergoing a spectacular renaissance [2]. Thanks to the continuous increase in computing capabilities, microscopic methods based on nuclear density functional theory (DFT) have become very competitive with the phenomenological models that were prevalent until now [3]. The application of these techniques has given truly novel insights into the fission process, such as unveiling the role of shell effects in setting the dominant fission modes [4], analyzing the dissipative nature of the fission process [5–8], and predicting the spin of fission fragments [9–11]. These recent developments are all the more important as simultaneous progress in simulations of nucleosynthesis have created a strong demand for predictive and complete models of fission applicable across the entire chart of isotopes [12–14]. A more predictive model of fission may also be key to understanding the nuclear reactor antineutrino anomaly [15,16]. Such applications make it especially important to build comprehensive models of fission that can describe the entire chain of events occurring in the process, from the formation of the compound nucleus to the β decay and delayed emission of the fission products [17–19].

Until now, the majority of fission studies, whether based on DFT or phenomenological mean-field models, have been restricted to even-even fissioning nuclei. There are a few notable exceptions: in Refs. [20,21], fission barrier heights of ^{235}U and ^{239}Pu were computed in the Skyrme Hartree-Fock theory with pairing correlations treated at the Bardeen-Cooper-Schrieffer

(BCS) approximation, including a full treatment of the time-odd terms for several different configurations of the odd neutron. In Ref. [22], the one-dimensional fission path and spontaneous fission half-life of ^{235}U for two different values of the spin projection $K = 1/2$ and $K = 7/2$ were computed at the Hartree-Fock-Bogoliubov (HFB) approximation with the Gogny force. This analysis was extended in Ref. [23], where similar calculations were performed for the uranium and plutonium isotopic chains. Even though the details of these studies differ, they all highlighted the fact that fission barrier heights, and by extension, the potential energy surface, vary substantially with the configuration occupied by the odd particle. While this has an obvious impact on calculated spontaneous fission half-lives, which are extremely sensitive to the shape and height of the fission barrier, one should also expect an effect on fission fragment distributions. Moreover, the spin dependence of the potential energy surface in odd-mass nuclei has an interesting consequence for neutron-induced fission since upon formation the spin distribution of the compound nucleus acquires a sizable spread. The characteristics of the entrance channel should therefore have a visible impact on the distribution of fission fragments.

The goal of this paper is to outline a theoretical framework based on the HFB theory with blocking and the time-dependent generator coordinate method with the Gaussian overlap approximation (TDGCM+GOA) to compute the charge and mass distributions of fission fragments for an odd-mass compound nucleus. We confirm the important impact of the blocked configurations on nuclear deformation properties. By computing two-dimensional potential energy surfaces, we give the first microscopic calculation of fission fragment distributions for different blocked configurations. Finally, we use the coupled channel reaction formalism to include

*schunck1@llnl.gov

information about the entrance channel in the determination of the fission fragment distributions.

Section II gives an overview of the theoretical framework. Most of it is well known and presented in textbooks [24]. The one exception is the generalization of the formula for the collective inertia to the case of an odd nucleus. In Sec. III, we summarize the results of static HFB calculations, both one-dimensional fission paths and two-dimensional potential energy surfaces. Section IV discusses the methodology adopted to incorporate calculated spin distributions of the compound nucleus into predictions of fission fragment distributions and shows results for uranium isotopes.

II. THEORETICAL FRAMEWORK

In this article, we focus on calculations of fission product yields from neutron-induced fission. After absorbing the incident neutron, the resulting compound nucleus can decay through different channels, either by emitting particles (primarily neutrons or γ rays) or by fissioning. From a theoretical point of view, fission is described as a large-amplitude collective motion that drives the nucleus from a near-spherical shape to the scission point. Typically each fission event leads to a pair of fission fragments; ternary fission will not be considered here. We distinguish between the yields at two different times following Refs. [25,26]. The fission fragment charge and mass distributions that one would obtain immediately after scission will be referred to as *primary fission fragment distributions*. The term primary fission fragments means that the nuclear species formed have yet to emit any prompt particles. One can define primary charge $Y(Z)$, mass $Y(A)$, or isotopic $Y(Z, A)$ distributions.

The prompt emission of neutrons and γ rays from the fission fragments changes the relative abundance of each isotope. At the end of this prompt de-excitation phase, which typically takes of the order of 10^{-16} s after scission, the new distributions of fission fragments are called the *independent yields*. Again, one distinguishes between independent charge $Y_{\text{ind.}}(Z)$, mass $Y_{\text{ind.}}(A)$, and isotopic $Y_{\text{ind.}}(Z, A)$ yields.

A. Treatment of the entrance channel

For the heavy systems we are addressing in this work, the number of degrees of freedom involved in a neutron-induced reaction is very large, as attested by the high level density at the relevant excitation energies (typically of the order of 10^6 MeV^{-1} around the neutron separation energy). In this regime, a statistical description of the process is known to work well [27–31], and the states populated in the reaction are described in terms of compound nucleus formation. In particular, Bohr's hypothesis is usually applied, according to which the way a compound nucleus decays is independent of how it was formed. Aside from the explicit consideration of small deviations from this hypothesis in terms of the so-called width fluctuations that correlate entrance and exit channels, there is an important caveat: the energy, angular momentum, and parity of the entrance channel are exactly preserved in the exit channel. Since the decay branching ratios corresponding to the different decay modes depend strongly on these con-

served quantities, it is essential to predict the population of the compound nucleus states in terms of the energy, spin, and parity distributions as the neutron is absorbed.

The absorption process is described within a direct reaction scheme in terms of a coupled-channels reaction formalism. Under the assumption that the target nucleus is described by a rigid rotor Hamiltonian (see, e.g., [32]), the incident neutron is coupled to the intrinsic structure of the target nucleus through the imaginary part of the optical potential, as well as through the direct excitation of the members of the ground-state rotational band. The wave function of the composite system formed by the incident neutron and the target is expanded in terms of the states $\Phi_{I_n}(\xi)$ of the target ground-state rotational band with spin I_n,

$$\Psi_{JM}(\mathbf{r}, \xi) = \sum_{n} \sum_{j_n l_n} \frac{4\pi}{k_n r} \phi_n(r) \big[\chi_{j_n l_n}(\hat{r}, \sigma) \Phi_{I_n}(\xi) \big]_M^J, \quad (1)$$

where $\mathbf{r}$ is the neutron-target relative coordinate and ξ denotes the set of coordinates associated with the target. We note $n \equiv \{n; JM j_n l_n\}$, where n indexes the components of its (J, M) channel, J and M are the total spin and its projection, j_n and l_n are the total and orbital angular momentum of the neutron, and k_n its wave number. The radial part of the channel wave function is noted $\phi_n(r)$ while $\chi_{j_n l_n}(\hat{r}, \sigma)$ refers to its angular and spin part (σ is the neutron spin). The square brackets indicate angular momentum coupling of j_n and I_n to total spin and projection J, M. The set of coupled differential equations obeyed by the channel wave functions $\phi_n(r)$ can be obtained by projecting the many-body Schrödinger equation on the target rotational states [33],

$$\frac{\hbar^2}{2m} \left(\frac{d^2}{dr^2} + \frac{l_n(l_n + 1)}{r^2} + U(r) - k_n^2 \right) \phi_n(r)$$
$$= -\sum_{m \neq n} V_{nm}(r; \boldsymbol{\beta}) \phi_m(r), \quad (2)$$

where $U(r)$ is a complex optical potential. For a rigid rotor, the coupling potentials $V_{nm}(r; \boldsymbol{\beta})$ depend on the deformation parameters $\boldsymbol{\beta} \equiv \{\beta_2, \beta_4, \beta_6\}$ of the mean-field potential in the target. Since we are using the coupling scheme developed in [34] restricted to transitions within the ground state rotational band, thus neglecting transitions between bands, we will only consider here deformations with even multipolarity. The coupling potentials thus read

$$V_{nm}(r; \boldsymbol{\beta}) = \sum_{\lambda} v_{\lambda}(r; \beta_{\lambda}) B_{\lambda}(n, m) A_{\lambda}(n, m), \quad (3)$$

where $B_{\lambda}(n, m)$ and $A_{\lambda}(n, m)$ are geometrical coefficients depending on the spins of the states n and m (see [33]),

$$A_{\lambda}(n, m) = \frac{1}{\sqrt{4\pi}} (-1)^{J - \frac{1}{2} - I_m + j_n + j_m + \frac{1}{2}(l_m - l_n)}$$
$$\times \sqrt{(2j_m + 1)(2j_n + 1)} \left\langle j_n j_m \ - \frac{1}{2} \frac{1}{2} \middle| \lambda \, 0 \right\rangle$$
$$\times W(j_n I_n j_m I_m; J\lambda), \quad (4)$$

$$B_{\lambda}(n, m) = \sqrt{(2I_n + 1)} \langle I_m \lambda \, M \, 0 | I_n M \rangle. \quad (5)$$

The functions $v_\lambda(r; \beta_\lambda)$ are the coefficients of the multipole expansion of a deformed Woods-Saxon potential with standard real and imaginary surface terms, as well as a real spin-orbit term; for details, see [34]. The geometry and energy dependence of this potential, as well as the deformation parameters $\boldsymbol{\beta}$, were fitted to reproduce neutron elastic scattering and total reaction cross sections in actinides [34].

The set of coupled differential equations (2) is solved for the neutron wave functions $\phi_n(r)$. The phase shifts δ_{lJ} corresponding to the elastic wave function are then obtained by matching the components $\phi_0(r)$ of the partial wave expansion of the elastic scattering wave at a large enough radius R to the spherical Bessel $[j_l(r)]$ and Neumann $[y_l(r)]$ functions,

$$\phi_0(R) = \cos(\delta_{lJ}) j_l(R) + \sin(\delta_{lJ}) y_l(R). \qquad (6)$$

The radius R should be larger than the range of the nuclear interaction between the target and the neutron, in our numerical calculations we have used $R = 20$ fm.

The scattering matrix $S_{l,J\pi} = e^{2i\delta_{lJ}}$ for each spin J and parity π, and partial wave l, can then be used to determine the transmission coefficient $T_{J\pi}$ associated with the formation of the compound nucleus according to the expression

$$T_{J\pi} = 1 - \sum_l |S_{l,J\pi}|^2. \qquad (7)$$

In Sec. IV A this transmission coefficient will be taken as the probability $P_{\text{th.}}(J^\pi)$ of having the compound nucleus in a state with spin J and parity π.

B. Large-amplitude collective motion for odd nuclei

One of the main goals of this work is to determine the primary fission fragment distributions $Y(Z)$ and $Y(A)$ of an odd-mass fissioning nucleus. To this end, we work within the global framework of the energy density functional (EDF) theory [24]. Fission fragment distributions are computed in a three-step process: (i) the potential energy surface (PES) of the nucleus is computed in a small space of collective variables within the static HFB theory; (ii) the time-evolution of a collective wave packet on this PES is simulated with the time-dependent generator coordinate method under the Gaussian overlap approximation [35]; (iii) the actual fission fragment charge and mass distributions are extracted by computing the flux of the collective wave packet through the scission line or surface. This approach was first proposed in the 1980s at CEA Bruyères-le-Châtel [36–38] with early applications in the 2000s [39–41] and it is presented in great detail in Refs. [42–45]. In the following, we only describe the extension of this formalism to odd-mass nuclei.

1. Blocking prescription

Nuclei with odd numbers of particles are computed at the HFB approximation with the blocking prescription [46–48]. The ansatz for the many-body state thus reads

$$|\Phi\rangle = \beta_\alpha^\dagger \prod_k \beta_k |0\rangle , \qquad (8)$$

where $|0\rangle$ is the particle vacuum and β_k are the quasiparticle annihilation operators as determined by the Bogoliubov

transformation. In practice, the HFB equation with blocking is solved by substituting the column vectors $(U_\alpha, V_\alpha) \leftrightarrow (V_\alpha^*, U_\alpha^*)$ for the quasiparticle α one wishes to block [24,46]. This procedure is performed at each iteration of the self-consistent loop. The density matrix and pairing tensor in configuration space become

$$\rho_{ij}^{B,\alpha} = (V^* V^T)_{ij} + U_{i\alpha} U_{j\alpha}^* - V_{i\alpha}^* V_{j\alpha}, \qquad (9a)$$

$$\kappa_{ij}^{B,\alpha} = (V^* U^T)_{ij} + U_{i\alpha} V_{j\alpha}^* - V_{i\alpha}^* U_{j\alpha}. \qquad (9b)$$

The exact implementation of the blocking prescription breaks time-reversal symmetry and depends on the self-consistent symmetries [49]. For this reason, one often employs the equal filling approximation (EFA) where time-reversal symmetry is explicitly enforced [50]. Detailed comparisons of the energies of blocking configurations near the Fermi level showed that the error incurred when using the EFA does not exceed a few keV [48,49]. As demonstrated in Ref. [50], the EFA can be thought of as a special statistical mixture of one-quasiparticle states. The density matrices are thus modified to read as

$$\rho_{ij}^{\text{EFA},\alpha} = (V^* V^T)_{ij} + \tfrac{1}{2}(U_{i\alpha} U_{j\alpha}^* - V_{i\alpha}^* V_{j\alpha} \\ + U_{i\bar{\alpha}} U_{j\bar{\alpha}}^* - V_{i\bar{\alpha}}^* V_{j\bar{\alpha}}), \qquad (10a)$$

$$\kappa_{ij}^{\text{EFA},\alpha} = (V^* U^T)_{ij} + \tfrac{1}{2}(U_{i\alpha} V_{j\alpha}^* - V_{i\alpha}^* U_{j\alpha} \\ + U_{i\bar{\alpha}} V_{j\bar{\alpha}}^* - V_{i\bar{\alpha}}^* U_{j\bar{\alpha}}). \qquad (10b)$$

In this work, the selection of quasiparticle states to block follows the automated procedure outlined in Ref. [51]. From the HFB solution in the even-even neighbor, the code identifies an initial set $\mathcal{B}$ of blocking candidates α within a small energy window around the Fermi energy by imposing the condition $|E_\alpha - E_0| \leqslant \Delta E$, where E_0 is the energy of the lowest quasiparticle and ΔE is the energy window. This procedure is applied for each Ω block. At each iteration n, the code computes the overlap $O_{\alpha\alpha'}$ between the blocked state $\alpha \equiv \alpha^{(n-1)}$ at the previous iteration and each quasiparticle state in the same Ω block, $O_{\alpha\alpha'} = \sum_i (U_{i\alpha} U_{i\alpha'} + V_{i\alpha} V_{i\alpha'})$. The quasiparticle α' with the maximum overlap defines the updated version of α at iteration n, $\alpha^{(n)} = \alpha'$.

Applying this blocking prescription at each point **q** of the PES gives a set of N_q blocking potential energies, $\mathcal{S}_q \equiv \{V_\alpha(\mathbf{q})\}_{\alpha=1,...,N_q}$. Note that the number N_q of such configurations is not the same everywhere on the PES, since the blocking criterion is based on a fixed energy window ΔE. Similarly, the numbers of blocked states N_Ω with $\Omega = 1/2$, $\Omega = 3/2, \ldots$, within a given set $\mathcal{S}_q$ are not identical. Often the number of blocked states is such that $N_{1/2} \geqslant N_{3/2} \geqslant \ldots$.

2. Time-dependent generator coordinate method

In this work, we assume that the large-amplitude collective dynamics of the fissioning nucleus can be approximated by the time-dependent generator coordinate method (TDGCM) under the Gaussian overlap approximation (GOA). Let us recall that the fundamental hypothesis of this method is that the quantum state $|\text{GCM}(t)\rangle$ that describes the fissioning system is a time-dependent linear superposition of static states at

different deformations

$$|\text{GCM}(t)\rangle = \int d\mathbf{q}\,|\Phi(\mathbf{q})\rangle\,f(\mathbf{q}, t), \tag{11}$$

where f is a complex-valued function that defines the superposition at each time t and $|\Phi(\mathbf{q})\rangle$ is a constrained HFB state. Using the additional hypotheses of the GOA, the TDGCM+GOA equation of motion reads

$$i\hbar \frac{\partial g(\mathbf{q}, t)}{\partial t} = [\boldsymbol{H}_{\text{coll.}}(\mathbf{q}) + i\boldsymbol{A}_{\text{coll.}}(\mathbf{q})]\,g(\mathbf{q}, t), \tag{12}$$

where the complex-valued function $g(\mathbf{q}, t)$, equivalent to $f(\mathbf{q}, t)$, contains all the information about the dynamics of the system and $\boldsymbol{A}_{\text{coll.}}(\mathbf{q})$ is a real-valued field that is added to avoid reflection on the boundaries of the deformation domain [52]. The collective Hamiltonian $\boldsymbol{H}_{\text{coll.}}(\mathbf{q})$ is a local linear operator acting on $g(\mathbf{q}, t)$,

$$\boldsymbol{H}_{\text{coll.}}(\mathbf{q}) \equiv -\frac{\hbar^2}{2\gamma^{1/2}(\mathbf{q})} \sum_{\mu\nu} \frac{\partial}{\partial q_\mu} \gamma^{1/2}(\mathbf{q}) B_{\mu\nu}(\mathbf{q}) \frac{\partial}{\partial q_\nu} + V(\mathbf{q}) \tag{13}$$

with $B_{\mu\nu}(\mathbf{q})$ the components of the collective inertia tensor, $V(\mathbf{q})$ the potential energy, which is the sum of the HFB energy and some zero-point energy corrections, and γ is the GCM metric [53].

Equation (12) is derived from the Hill-Wheeler-Griffin equation of the GCM after applying the GOA [35]. The derivation does require that the generator states $|\Phi(\mathbf{q})\rangle$ are pure states with the structure of quasiparticle vacuum [24]. In the EFA, this is not satisfied since the system is in fact described by a (very specific) statistical density operator. However, it is possible to compute every ingredient of Eq.(13) (potential energy, zero-point energy corrections, and collective inertia) for statistical ensembles through the extension of the adiabatic time-dependent Hartree-Fock-Bogoliubov (ATDHFB) at finite temperature. Therefore, we adopt the pragmatic point of view of using Eq. (12) as the equation of motion with inputs determined from the finite-temperature ATDHFB theory—with statistical occupations given by the EFA prescription. Since the (TD)GCM formalism has not been extended to finite temperature yet, this is a reasonable compromise that has already been applied to study the structure of the collective inertia mass tensor as a function of temperature [54], thermal spontaneous fission rates [55], the dependency of primary fission fragment distributions on excitation energy [56], and to estimate dissipation effects in fission fragment distributions [57]. In spite of these examples, the full derivation of the ATDHFB collective inertia tensor $B_{ij}(\mathbf{q})$ at finite temperature has never been presented. The special case of the ATDHFB+BCS inertia was derived in Refs. [58,59] by replacing expectation values of observables in the zero-temperature cranking model formula by ensemble averages and the full, correct ATDHFB result was given without proof in Ref. [54]. Therefore, we demonstrate below how to obtain the formula for the finite-temperature ATDHFB collective inertia tensor.

(a) ATDHFB equations. The starting point of the derivation is the Liouville equation for the density operator

$\mathcal{D}$ [60]. Applying the statistical Wick theorem yields the finite-temperature time-dependent Hartree-Fock-Bogoliubov (TDHFB) equation, which is formally equivalent to the zero-temperature TDHFB equation, $i\hbar\dot{\mathcal{R}} = [\mathcal{H}, \mathcal{R}]$ [61]. Following the ideas of ATDHF [62], we then write the TDHFB generalized density $\mathcal{R}(t) = e^{i\chi(t)}\mathcal{R}^{(0)}(t)e^{-i\chi(t)}$, where $\chi(t)$ is a quadratic form of single-particle creation and annihilation operators [61]. Assuming the operator $\chi(t)$ is small, one can make a Taylor expansion of the TDHFB generalized density matrix, $\mathcal{R}(t) = \mathcal{R}^{(0)}(t) + \mathcal{R}^{(1)}(t) + \mathcal{R}^{(2)}(t)$, for example, $\mathcal{R}^{(1)} = i[\chi(t), \mathcal{R}^{(0)}(t)]$. Plugging these two Taylor expansions into the finite-temperature TDHFB equation and separating contributions that are time-even from the ones that are time-odd gives a set of coupled equations that are formally analogous to the zero-temperature ATDHFB equations

$$i\hbar\dot{\mathcal{R}}^{(0)} = [\mathcal{H}^{(0)}, \mathcal{R}^{(1)}] + [\mathcal{H}^{(1)}, \mathcal{R}^{(0)}], \tag{14a}$$

$$\begin{aligned} i\hbar\dot{\mathcal{R}}^{(1)} = {}& [\mathcal{H}^{(0)}, \mathcal{R}^{(0)}] + [\mathcal{H}^{(0)}, \mathcal{R}^{(2)}] \\ & + [\mathcal{H}^{(1)}, \mathcal{R}^{(1)}] + [\mathcal{H}^{(2)}, \mathcal{R}^{(0)}]. \end{aligned} \tag{14b}$$

In Eqs. (14a)–(14b), the matrices $\mathcal{H}^{(n)}$ represent the finite-temperature HFB (FT-HFB) matrices at order n, i.e., they depend on the order-n density matrices $\rho^{(n)}(t)$ and $\kappa^{(n)}(t)$ that enter the generalized densities $\mathcal{R}^{(n)}(t)$,

$$\mathcal{R}^{(0)}(t) = \begin{pmatrix} \rho^{(0)} & \kappa^{(0)} \\ -\kappa^{(0)*} & 1 - \rho^{(0)*} \end{pmatrix}, \tag{15}$$

$$\mathcal{R}^{(n)}(t) = \begin{pmatrix} \rho^{(n)} & \kappa^{(n)} \\ -\kappa^{(n)*} & -\rho^{(n)*} \end{pmatrix}. \tag{16}$$

We now introduce the TDHFB quasiparticle basis, which diagonalizes at each time the zero-order, finite-temperature $\mathcal{R}^{(0)}(t)$ density matrix. In that basis, $\mathcal{R}^{(0)}(t)$ takes the form

$$\tilde{\mathcal{R}}^{(0)}(t) = \begin{pmatrix} f(t) & 0 \\ 0 & 1 - f(t) \end{pmatrix} \tag{17}$$

with $f_{kl}(t)$ the statistical occupation factors. In the following, the tilde indicates that a matrix is written in the TDHFB quasiparticle basis.

(b) Energy to second order. The next step is to obtain a closed-form expression for the total energy of the system that only depends on the operator $\chi(t)$. This is achieved by first expanding the TDHFB energy in terms of the matrices $\mathcal{R}^{(n)}$. One obtains

$$E = E_{\text{HFB}} + \tfrac{1}{2}\text{tr}(\mathcal{H}^{(0)}\mathcal{R}^{(2)}) + \tfrac{1}{4}\text{tr}(\mathcal{H}^{(1)}\mathcal{R}^{(1)}). \tag{18}$$

We can then use the commutators that relate each of the $\mathcal{R}^{(n)}$ to $\chi(t)$ to obtain an expression of E as a function of $\chi(t)$ only. Even when working in the TDHFB quasiparticle basis, the full calculation is rather lengthy because of the term proportional to $\mathcal{H}^{(1)}$, which depends on $\mathcal{R}^{(1)}$ indirectly through its components $\rho^{(1)}$ and $\kappa^{(1)}$ and corresponds to the off-diagonal terms of the FT-QRPA matrix [60]. Since we work at the cranking approximation, we neglect it. It is then relatively straightforward to show that the total energy reduces to

$$E = E_{\text{HFB}} + \tfrac{1}{4}\vec{\chi}^\dagger \mathcal{M} \vec{\chi}, \tag{19}$$

where $\bar{\chi}$ is the linearized version of the matrix of the operator χ in the TDHFB quasiparticle basis,

$$\tilde{\chi} = \begin{pmatrix} \tilde{\chi}^{11} & \tilde{\chi}^{12} \\ \tilde{\chi}^{21} & \tilde{\chi}^{22} \end{pmatrix} \quad \Rightarrow \quad \vec{\chi} = \begin{pmatrix} \tilde{\chi}^{11} \\ \tilde{\chi}^{12} \\ \tilde{\chi}^{21} \\ \tilde{\chi}^{22} \end{pmatrix}, \tag{20}$$

and $\mathcal{M}$ is the FT-QRPA matrix in the cranking approximation. In that same linearized TDHFB basis, it can be written $\mathcal{M} = \mathbb{E}\mathbb{F}$ with

$$\mathbb{E} = \begin{pmatrix} (E_k - E_l) & & & \\ & (E_k + E_l) & & \\ & & -(E_k + E_l) & \\ & & & -(E_k - E_l) \end{pmatrix}$$

and

$$\mathbb{F} = \begin{pmatrix} -(f_k - f_l) & & & \\ & (1 - f_k - f_l) & & \\ & & -(1 - f_k - f_l) & \\ & & & (f_k - f_l) \end{pmatrix}.$$

In these last two expressions, terms like $E_k - E_l$ stand for the matrix $\tilde{E}$ with elements $\tilde{E}_{kl} = E_k - E_l$ with E_k the quasiparticle energies.

(c) Adiabatic approximation. Starting from Eqs.(14a),(14b) and continuing to work in the TDHFB quasiparticle basis, one can show that

$$\hbar \vec{\dot{\mathcal{R}}}^{(0)} = \mathbb{E}\mathbb{F}\vec{\chi} = \mathcal{M}\vec{\chi}, \tag{21}$$

where $\vec{\dot{\mathcal{R}}}^{(0)}$ is, again, the linearized matrix of the operator $\dot{\mathcal{R}}^{(0)}$ in the TDHFB basis. The total energy thus reads

$$E = E_{\text{HFB}} + \frac{\hbar^2}{4} \vec{\dot{\mathcal{R}}}^{(0)\dagger} \mathcal{M}^{-1} \vec{\dot{\mathcal{R}}}^{(0)}. \tag{22}$$

As is customary in practical applications of the ATDHF or ATDHFB theory [62], we then introduce a (small) set of collective variables $\mathbf{q} \equiv (q_1, \ldots, q_N)$ and assume that the densities $\mathcal{R}^{(0)}(t)$ vary in time only through changes in these collective variables,

$$\dot{\mathcal{R}}^{(0)} = \sum_\mu \dot{q}_\mu \frac{\partial \mathcal{R}^{(0)}}{\partial q_\mu}. \tag{23}$$

In physics terms, this statement is the equivalent of the Born-Oppenheimer approximation: the nuclear dynamics is confined to a collective space. Additionally, we approximate the solutions of the finite-temperature HFB equation constrained on the expectation value $\mathbf{q}$ of the collective variables by the static densities $\mathcal{R}^{(0)}$. In other words, the collective space that contains the nuclear dynamics is precalculated as a series of FT-HFB calculations. Let us emphasize here that these approximations are exactly the same as the ones underpinning the zero-temperature expressions of the ATDHFB collective inertia that are commonly used in the literature.

(d) Local approximation. The final stage of the derivation consists in expressing $\partial \mathcal{R}^{(0)}/\partial q_\mu$ locally at point $\mathbf{q}$. Since we have assumed that the density $\mathcal{R}^{(0)}$ is the solution of the FT-HFB equation with constraints $\mathbf{q}$, it satisfies $[\mathcal{H}^{(0)} - \sum_\mu \lambda_\mu \hat{Q}_\mu, \mathcal{R}^{(0)}] = 0$ with λ_μ the Lagrange parameter associated with the constraint operator $\hat{Q}_\mu$. We collect all such parameters into the vector $\boldsymbol{\lambda} = (\lambda_1, \ldots, \lambda_N)$. We then express

that this equation must be satisfied for small variations of the density, that is, when

$$\mathcal{R}^{(0)} \to \mathcal{R}^{(0)} + \mathcal{R}^{(1)},$$
$$\mathcal{H}^{(0)} \to \mathcal{H}^{(0)} + \mathcal{H}^{(1)},$$
$$\lambda_\mu \to \lambda_\mu + \delta\lambda_\mu.$$

Introducing these expansions into the FT-HFB equation with constraints and taking advantage of the quasiparticle basis, some simple algebra leads to the following relation: $\vec{\mathcal{R}}^{(1)} = -\delta\boldsymbol{\lambda} \cdot \mathbb{E}^{-1}\mathbb{F}\vec{\mathbf{Q}}$, where $\vec{\mathbf{Q}} \equiv (\vec{Q}_1, \ldots, \vec{Q}_N)$ is a vector containing the linearized matrix $\vec{Q}_\mu$ of the constraint operator in the TDHFB quasiparticle basis. To clarify, the condensed notation stands for

$$\vec{\mathcal{R}}^{(1)} = -\delta\boldsymbol{\lambda} \cdot \mathbb{E}^{-1}\mathbb{F}\vec{\mathbf{Q}}$$

$$= -\sum_\mu \delta\lambda_\mu \sum_{kl} \left[\frac{f_k - f_l}{E_k - E_l} \tilde{Q}^{11}_{\mu;kl} - \frac{1 - f_k - f_l}{E_k + E_l} \tilde{Q}^{12}_{\mu;kl} \right.$$
$$\left. - \frac{1 - f_k - f_l}{E_k + E_l} \tilde{Q}^{21}_{\mu;kl} + \frac{f_k - f_l}{E_k - E_l} \tilde{Q}^{22}_{\mu;kl} \right].$$

We apply the chain rule to write

$$\frac{\partial \mathcal{R}^{(0)}}{\partial q_\mu} = \sum_\alpha \frac{\mathcal{R}^{(0)}}{\lambda_\alpha} \frac{\lambda_\alpha}{q_\mu}. \tag{24}$$

At this point, we identify the small variations of the generalized density with the first-order variations $\mathcal{R}^{(1)}$, i.e., $\delta\mathcal{R}^{(0)} = \mathcal{R}^{(1)}$. We then obtain the variations $\delta\lambda_a$ simply by recalling that in the TDHFB quasiparticle basis,

$$q_\mu = \tfrac{1}{2}\text{tr}(\mathbf{Q}_\mu) + \tfrac{1}{2}\text{tr}(\mathbf{Q}_\mu \mathcal{R}^{(0)}) \Rightarrow \delta q_\mu = \tfrac{1}{2}\text{tr}(\mathbf{Q}_\mu \mathcal{R}^{(1)}). \tag{25}$$

The variation can also be written $\delta q_\mu = \tfrac{1}{2}\vec{Q}^\dagger_\mu \vec{\mathcal{R}}^{(1)}$. Using the previous relationship between $\vec{\mathcal{R}}^{(1)}$ and $\vec{\mathbf{Q}}$, we can find that

$$\delta\lambda_\nu = 2\sum_\alpha [\mathsf{M}]^{-1}_{\nu\alpha} \delta q_\alpha \tag{26}$$

with the moments $\mathsf{M}^{(K)} \equiv \vec{\mathbf{Q}}^\dagger \mathbb{E}^{-K} \mathbb{F} \vec{\mathbf{Q}}$, that is,

$$
\mathsf{M}_{\mu\nu}^{(K)} = \sum_{kl} \left[\tilde{Q}_{\mu;kl}^{11*} \frac{f_l - f_k}{(E_k - E_l)^K} \tilde{Q}_{\nu;kl}^{11} + \tilde{Q}_{\mu;kl}^{12*} \frac{1 - f_l - f_k}{(E_k + E_l)^K} \tilde{Q}_{\nu;kl}^{12} \right.
$$
$$
\left. + \tilde{Q}_{\mu;kl}^{21*} \frac{1 - f_l - f_k}{(E_k + E_l)^K} \tilde{Q}_{\nu;kl}^{21} + \tilde{Q}_{\mu;kl}^{22*} \frac{f_l - f_k}{(E_k - E_l)^K} \tilde{Q}_{\nu;kl}^{22} \right].
$$

The time variations of $\mathcal{R}^{(0)}$ thus become

$$
\dot{\vec{\mathcal{R}}}^{(0)} = 2 \sum_{\alpha\beta} \dot{q}_\beta [\mathsf{M}^{(1)}]_{\alpha\beta}^{-1} \mathbb{E}^{-1} \mathbb{F} \vec{Q}_\beta \tag{27}
$$

leading to the total energy taking the form

$$
E_2 = \frac{1}{2} \sum_{\mu\nu} \mathsf{M}_{\mu\nu} \dot{q}_\mu \dot{q}_\nu \tag{28}
$$

with

$$
\mathsf{M} = 2\hbar^2 [\mathsf{M}^{(1)}]^{-1} \mathsf{M}^{(3)} [\mathsf{M}^{(1)}]^{-1}. \tag{29}
$$

Apart from a factor of 2, this formula is the same as the zero-temperature result. The main difference lies in the definition of the moments $\mathsf{M}_{\mu\nu}^{(K)}$, which depend explicitly on the Fermi-Dirac statistical occupations. In the case of the EFA, we recall that $f_k = 0$ except $f_\alpha = f_{\bar{\alpha}} = 1/2$.

III. STATIC POTENTIAL ENERGY SURFACES

As mentioned earlier, we assume in this work that axial and time-reversal symmetries are conserved. In addition to accelerating calculations substantially, this hypothesis greatly facilitates the implementation of the blocking prescription as discussed in Sec. II B 1. Enforcing axial symmetry has two main consequences: (i) K-mixing between states is not possible and (ii) the height of the first fission barrier will be systematically overestimated by about 1–1.5 MeV [63–69].

All calculations were performed with the code HFBTHO [70]. We use a deformed harmonic oscillator (HO) basis containing up to $N_{\text{shells}} = 30$ and truncated to $N_{\text{states}} = 1100$. The HO spherical frequency ω_0 and its axial deformation β_2 were adjusted based on the value of the quadrupole moment q_{20} following the empirical formula presented in [69]. We used the SkM* parametrization of the Skyrme functional [71] and a surface-volume, zero-range, density-dependent pairing interaction with a cut-off $E_{\text{cut}} = 60$ MeV. The neutron and proton strengths of the pairing force were adjusted to the three-point odd-even binding-energy difference for neutrons and protons separately in ^{236}U: $V_n = -255.250$ MeV and $V_p = -325.594$ MeV.

A. One-dimensional fission paths

We begin by recalling the role of quasiparticle blocking on one-dimensional fission paths. Calculations of fission barriers in odd-mass nuclei were first reported within the microscopic-macroscopic model using the blocking prescription [72–75]. Fully self-consistent calculations of fission paths in odd nuclei were performed for the Gogny force [22,23]. Most of these calculations focused on which K value gives the lowest fission barrier or lowest energy fission path. In Refs. [72,73], the
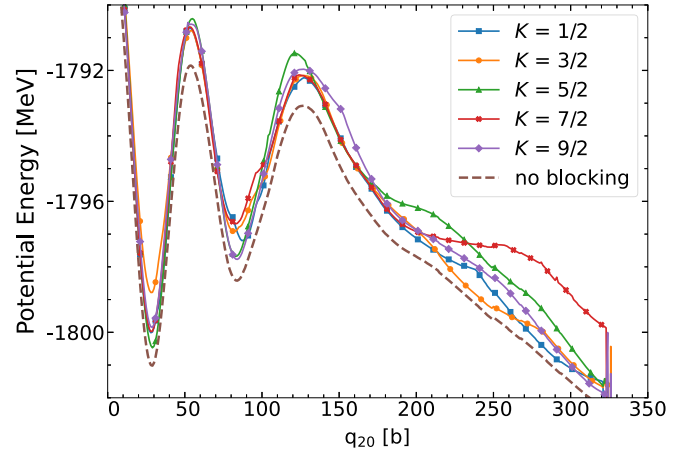

FIG. 1. Potential energy curves in ^{239}U as a function of the axial quadrupole moment q_{20} for different blocking configurations $K = 1/2, \ldots, 9/2$. The dashed line corresponds to a HFB calculation without the blocking prescription where the average number of particles is set to $Z_0 = 92$ and $N_0 = 147$.

authors investigated how changes in the blocking configuration affected the height of the barrier in a few select cases. Similar calculations were performed in the Hartree-Fock plus BCS formalism in Refs. [20,21], where the authors mentioned the consequences of the variations in fission barriers on quantities such as fission penetrabilities, which enter fission cross-section models.

In this section, we perform a more systematic exploration of the dependency of the full potential energy curves, from the ground state to the scission point, on different values of K. Figure 1 shows the example of blocking calculations in ^{239}U. For all K values included in the figure, the curve shows the energy of the lowest blocked configuration having that given K as a function of the expectation value of the axial quadrupole moment q_{20}. For comparison, we also show the result obtained in the no-blocking approximation, where the HFB solution for the odd nucleus has $K = 0$ because it is by construction a fully paired solution, only with the average particle number constrained to an odd value, here $\langle \hat{N} \rangle = 147$. We first note that the spin of the ground state (g.s.) is $K = 5/2$, which agrees with experimental assignment [76]. For ^{237}U, we found $K = 1/2$ for the g.s., which is also in agreement with experimental results. As already noticed in Refs. [22,23], the potential energy of blocked configurations is systematically higher than the no-blocking ones, which is a manifestation of the 'specialization' effect [21].

The comparison of the fission paths for different values of K show significant differences of the order of up to several MeV. Table I lists the height of the first fission barrier (E_A) and second fission barrier (E_B) as well as the excitation energy of the fission isomer (E_{FI}) for both ^{237}U and ^{239}U. The maximum difference reaches 1.28 MeV for E_A, 1.45 MeV for E_B, and 1.90 MeV for E_{FI} for ^{237}U, and 2.05 MeV for E_A, 2.39 MeV for E_B, and 1.54 MeV for E_{FI} for ^{239}U. Interestingly, and perhaps coincidentally, for both nuclei the mean value of E_A, E_B, and E_{FI} over the range of K values is quite close to the no-blocking result. These results confirm the conclusions in

TABLE I. Characteristic points of potential energy curves in ^{237}U and ^{239}U: height of the first barrier (E_A), of the second barrier (E_B), and excitation energy of the fission isomer (E_{FI}). The first five columns correspond to blocking configurations characterized by the K quantum number; the last column stands for the no-blocking option. All values are given in MeV.

	K	1/2	3/2	5/2	7/2	9/2	no blck.
^{237}U	E_A	9.17	7.89	9.09	9.00	8.17	8.54
	E_B	7.77	6.58	8.03	7.68	7.05	7.32
	E_{FI}	3.63	2.83	3.56	4.62	2.72	3.45
^{239}U	E_A	9.31	8.00	10.05	9.30	9.27	9.17
	E_B	7.78	6.63	8.99	7.83	7.88	7.94
	E_{FI}	2.86	2.34	3.49	3.88	2.67	3.09

Ref. [21]: since fission barrier heights enter in the form of an exponential in standard formulas for either spontaneous fission half-lives or fission cross sections [1,77], such differences are actually considerable.

There were many studies of the evolution of fission barriers with angular momentum [47,78–83]. Irrespective of the details of the theoretical model employed, all results pointed to the gradual decrease of the barriers due to the damping of shell effects. However, these analyses were focused on the total angular momentum J of even-even nuclei in a rather high-spin regime. Our axially symmetric blocking calculations only provide the eigenvalue K of $\hat{J}_z$ and we have $J \geqslant K$. Even though the K dependency of fission barriers in odd-mass nuclei as captured by blocking calculations is nonlinear—the height of the barrier is maximum at $K = 1/2$ for ^{237}U but at $K = 5/2$ for ^{239}U—one cannot exclude that full angular momentum projection would restore the order that one might expect from even-even nuclei ($E_A(J = \frac{1}{2}) \geqslant E_A(J = \frac{3}{2}) \geqslant \cdots$).

While relative differences, as quantified by the height of fission barriers, are large, absolute differences are much smaller: the energy at the top of the first barrier does not vary by more than 180 keV in ^{237}U and 280 keV in ^{239}U. In contrast, Fig. 1 shows that the energy in the ground-state potential well at $q_{20} \approx 30$ b, or in the descent from saddle to scission for $q_{20} > 170$ b, varies by up to several MeV. If such a pattern holds for multidimensional potential energy surfaces, these results suggest that blocking different K values could have an impact on the fission fragment distributions, not just fission probabilities.

Before finishing this section, we should point out a very general limitation of the blocking prescription in such potential energy surface calculations (even if it were implemented exactly by breaking time-reversal symmetry and axial symmetry). As recalled in Sec. II B 1, blocking calculations require a reference state, which is typically chosen as the neighboring even-even nucleus with either $N-1$ or $N+1$ particles, or sometimes the HFB solution for the no-blocking approximation. This prescription works very well everywhere except near scission. In one- or two-dimensional collective spaces, scission often takes the form of a discontinuity in the PES, as seen at $q_{20} \approx 325$ b in Fig. 1. If this discontinuity occurs at, say $q_{20}^{\text{disk.}} = q_0$ for the *reference* states, then the discontinuity
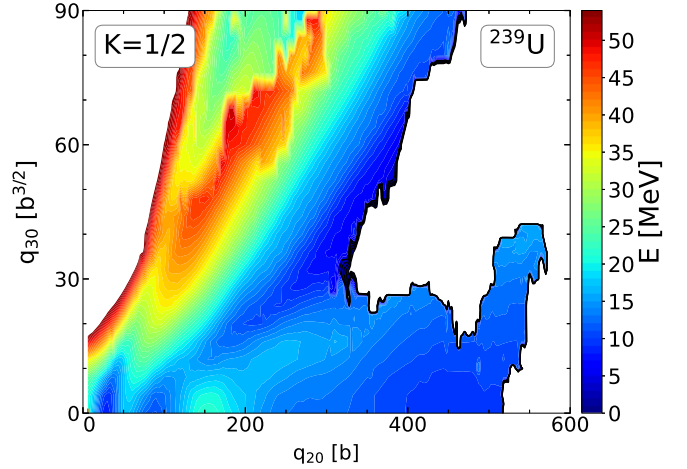

FIG. 2. Two-dimensional potential energy surface in ^{239}U as a function of the expectation value of the axial quadrupole (q_{20}) and axial octupole (q_{30}) moments for the $K = 1/2$ blocking configuration.

for *all* blocking configurations and K values built on these reference states must be such that $q_{20}^{\text{disk.}} \leqslant q_0$. In other words, the blocking scheme cannot produce a PES for some K value where scission would occur at larger values of q_{20} than in the reference state. The only case when such a situation is possible is if the collective space is large enough that scission takes place along a continuous path.

B. Two-dimensional potential energy surfaces

The one-dimensional potential energy curves of Sec. III A can provide useful information such as barrier heights for the calculation of spontaneous fission half-lives or fission cross sections. However, the determination of fission fragment distributions requires more collective degrees of freedom. In Fig. 2, we show the two-dimensional PES for the $K = 1/2$ configuration in ^{239}U. For this nucleus, blocking calculations for all K values at the point $\mathbf{q} = (q_{20}, q_{30})$ were initialized from the time-even reference state in ^{238}U at the same point $\mathbf{q}$. As mentioned in the previous section, this implies that configurations that are beyond scission in ^{238}U are also beyond scission in ^{239}U. In practice, we also found that for nearly all blocking solutions in ^{239}U, the scission line is identical to the one in ^{238}U. For this reason, the PES for $K = 1/2$ is, visually, nearly indistinguishable from the ones for $K = 3/2, \ldots, 9/2$—the color scale would not allow distinguishing differences in energy of the order of an MeV—so we choose to show only one such PES.

This PES is typical of most actinides [69,84–88]: the ground state is reflection-symmetric and located at around $q_{20} \approx 30$ b and the fission isomer at $q_{20} \approx 80$ b (details depend on the nucleus and the EDF). The second fission barrier is octupole-deformed and leads to the main fission valley. An additional fission path at much higher energy goes through very asymmetric shapes associated with cluster radioactivity.

The choice of the time-even reference solutions to initialize blocking calculations has another consequence. To generate the PES for ^{237}U, there are three obvious choices: start from the the PES of ^{236}U; from the PES of ^{238}U; or from the PES of
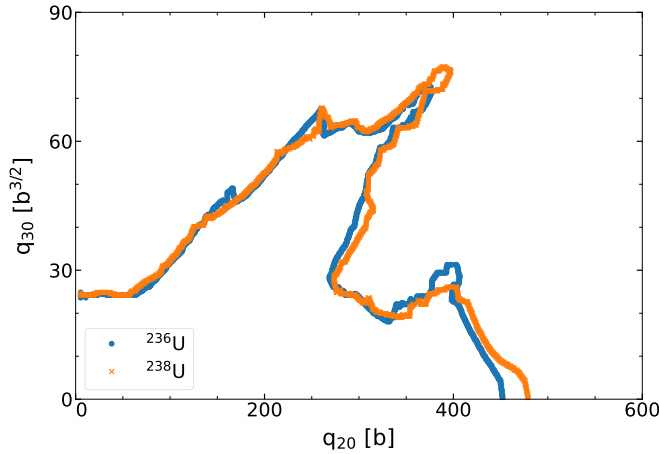
FIG. 3. Isoline with $q_N = 6.5$ in the two-dimensional potential energy surface of ^{236}U (blue circles) and ^{238}U (orange crosses).

^{237}U obtained without blocking. It is important to realize that the scission line in each of these three PES may be different. This is illustrated in Fig. 3, where the scission lines of both ^{236}U and ^{238}U are represented in the same figure. In this particular example, we adopted the condition $q_N = 6.5$ to define scission. The most likely fission fragments—the ones near the peaks of the fission fragment distribution–correspond to the region around $q_{20} \approx 300$–350 b and $q_{30} \approx 40$ b$^{3/2}$, i.e., to the right-hand side of the figure. Because scission configurations are not identical in each nucleus, blocking calculations in ^{237}U will give slightly different results depending on whether the PES for ^{237}U is initialized from the one in ^{236}U or ^{238}U.

These differences are minor, as illustrated in Figs. 4 and 5. Figure 4 shows the axial quadrupole and octupole deformation β_2 and β_3 of the fission fragments as a function of their mass. The deformations are defined from the multipole moments as $\beta_\lambda = 4\pi/(3AR^\lambda)Q_{\lambda 0}$ with $R = 1.2A^{1/3}$. Black
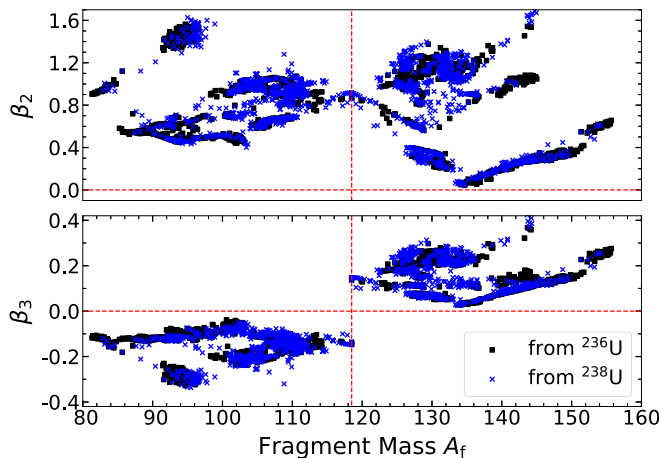

FIG. 4. Axial quadrupole (β_2) and octupole (β_3) deformation in the fission fragments in ^{237}U for $K = 1/2$. Black squares represent blocking calculations initialized from the PES in ^{236}U and blue crosses represent the ones initialized from the PES in ^{238}U. The vertical dashed line separates the light from the heavy fragments.
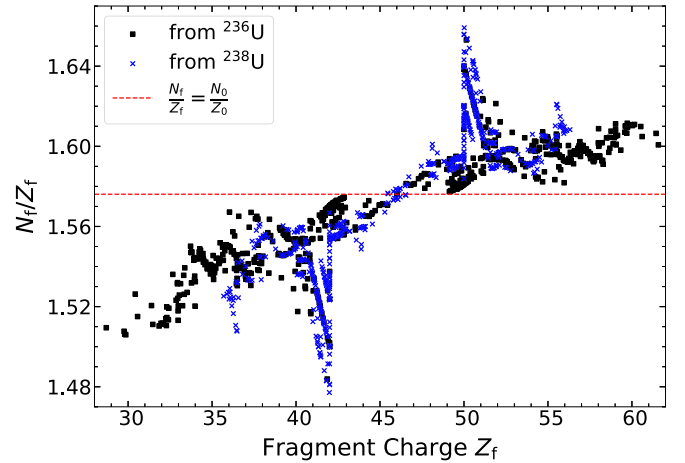

FIG. 5. Ratio of neutron over proton numbers in the fission fragments of ^{237}U as a function of the charge number of the fragment for $K = 1/2$. Black squares represent blocking calculations initialized from the PES in ^{236}U and blue crosses represent the ones initialized from the PES in ^{238}U. The dashed line corresponds to the ratio $N_0/Z_0 = 145/92$ of the fissioning nucleus.

squares correspond to blocking calculations initialized from the PES of ^{236}U, blue crosses to calculations initialized from the PES of ^{238}U. To increase statistics, we have retained all the configurations such that $1 \leqslant q_N \leqslant 8$ that have at least one of their nearest neighbors with $q_N < 1$. The ensemble of all such points give a very conservative estimate of the scission region. Overall, there are relatively few differences between both sets of deformations. As expected, we find that nearly all the heavy and the light fragments are octupole-deformed with values of β_3 of opposite signs for the light and heavy fragment. This implies that the two fragment smaller edge face each other, which simply results from the Coulomb repulsion that pushes protons apart from one another. Our results confirm earlier studies of fission in even-even actinide nuclei [84,85]. We also note the presence of very deformed fragments around $A_f \approx$ 125–145, such configurations are located near $q_{20} \approx 400$ b and $q_{30} \approx 25$–30 b$^{3/2}$ in a region plagued by discontinuities in the PES. We do not consider them truly physical.

Figure 5 completes this picture by showing the ratio of the number of neutrons to the number of protons in the fragments as a function of the charge number of said fragment. The dashed line represents the same ratio in the fissioning nucleus, $N_0/Z_0 = 145/92$. Results clearly show a charge polarization in the fission fragments, that is, the average number of neutrons deviates quite significantly from the unchanged charge distribution (UCD) approximation, which postulates that $N_f/Z_f = N_0/Z_0$. This justifies microscopically the empirical models used to simulate the charge polarization [89].

For the sake of completeness, we also computed the quantum localization indicator ℓ of the blocked quasiparticle (only in the case of ^{237}U) following the definitions in Refs. [69,90]. Although our results suggested that the percentage of well-localized blocked quasiparticles seemed to increase with K, they were not conclusive enough without a comprehensive study of scission configurations that would go beyond the

scope of this paper. Among the points worth investigating are possible differences between the quantum localization of the blocked quasiparticle and the one of other quasiparticles near the Fermi surface, and how results are dependent upon the definition of the scission configurations or the application of a unitary transformation on quasiparticles to approach asymptotic conditions.

IV. FISSION FRAGMENT DISTRIBUTIONS

This section summarizes our results on the fission fragment charge and mass distributions of the ^{236,238}U(n, f) reactions. Primary fission fragment distributions are extracted from the solution to the TDGCM+GOA equation (12) of Sec. II B. However, in the case of an odd-mass system, the application of the blocking procedure leads to a multisheet PES—one sheet for each $K = \langle \hat{J}_z \rangle$. We discuss how to set up the TDGCM+GOA equation in such a case and how to combine calculations for different K values to extract the yields. We then use the code FREYA [91,92] to model the de-excitation of the fission fragments and calculate the independent fission fragment mass and charge distributions.

A. Initial fission fragment distributions

Fission fragment distributions are extracted from the flux of the collective wave packet solution to Eq. (12) according to the general procedure described in detail in Ref. [52]. However, a few additional steps are needed to account for the fact that the compound nucleus can have different spin projections and that the probability of occupation of each of these configurations is given by the characteristics in the entrance channel.

In Sec. II B 1, we denoted by $V_K(\mathbf{q})$ the potential energy surface for the spin projection K of the odd nucleus. Since the collective nuclear Hamiltonian is rotationally invariant, we can compute the time-evolution using the TDGCM+GOA equation of motion for each K independently, that is,

$$i\hbar \frac{\partial g^{(K)}(\mathbf{q}, t)}{\partial t} = \left[\boldsymbol{H}_{\text{coll.}}^{(K)}(\mathbf{q}) + i \boldsymbol{A}_{\text{coll.}}^{(K)}(\mathbf{q}) \right] g^{(K)}(\mathbf{q}, t). \quad (30)$$

To infer the fission fragment distributions from the set of $g < K > (\mathbf{q}, t)$, we need to determine the initial probability that the compound nucleus is populated with spin projection K. In addition, solving Eq. (30) requires setting the initial state for the time evolution, i.e., $g < K > (\mathbf{q}, t = 0)$.

1. Initial conditions

The initial probability $P_{\text{th.}}(J^\pi)$ to populate a given total angular momentum J and parity π is determined using the coupled channel code FRESCO [93] which is part of the Lawrence Livermore National Laboratory–developed Hauser-Feshbach code YAHFC (version 3.67) [31]. The set of rotational states, potentials, and deformation parameters needed to define the coupled channels calculation were taken from Ref. [34]; see Sec. II A. The probability $p(J^\pi, K)$ to populate each K is determined using the equidistribution of the proba-
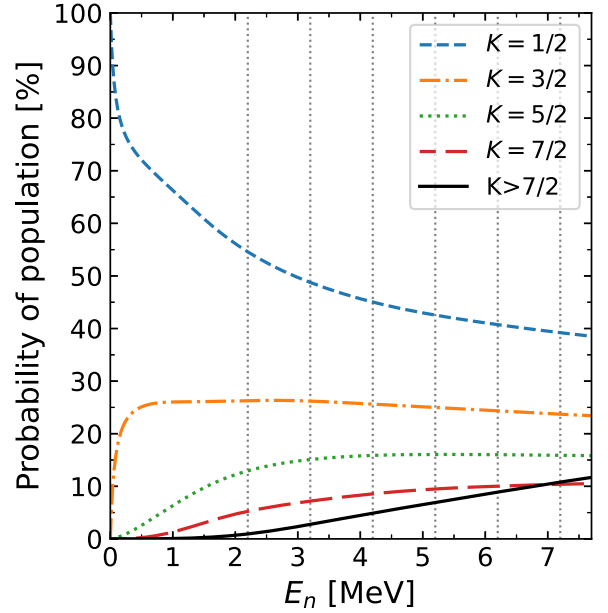

FIG. 6. Initial probability $p(K)$ to populate a given spin projection K in the ^{238}U(n, f) reaction as a function of the incident neutron energy E_n. Vertical dashed lines represent the energies considered in this work.

bilities

$$p(J^\pi, K) = \frac{P_{\text{th.}}(J^\pi)}{2J + 1}. \quad (31)$$

The probability of populating a given K is the sum of the probabilities for all valid J and π. Since we have $-J \leqslant K \leqslant J$, we get

$$p(K) = \sum_{J=|K|}^{J_{\text{max}}} \frac{P_{\text{th.}}(J^-) + P_{\text{th.}}(J^+)}{2J + 1}. \quad (32)$$

In principle, $p(K)$ should be obtained for $J_{\text{max}} \to +\infty$. In practice, we use a truncation of $J_{\text{max}} = \frac{33}{2}$, which is high enough to obtain a good approximation of the error associated with the other truncation in K. With this expression, we trivially have $p(K) = p(-K)$.

The nuclear Hamiltonian $\hat{H}$ is time-reversal invariant. Consequently, we get the same time-evolution and the same associated fission yields on a potential energy surface with values of K that differ by only a sign. Thus, we determine the time-evolution only for $K > 0$ with the population probability $p_\pm(K) = p(K) + p(-K) = 2p(K)$. The probability $p(K)$ we obtain with our approach is presented in Fig. 6 for the ^{238}U(n, f) reaction. We see that the contribution from configurations associated with $K > 7/2$ is always below 11% for the six neutron energies E_n considered here.

We define the initial state for the TDGCM+GOA time-evolution for each K using the prescription of Ref. [52]. We recall that this consists in first determining quasibound states $g_n^{(K)}$ located in the ground-state potential well, defined as solutions of the static GCM+GOA equation in an extrapolated potential, and then build the initial state as a superposition of these states, where the weights of the superposition are
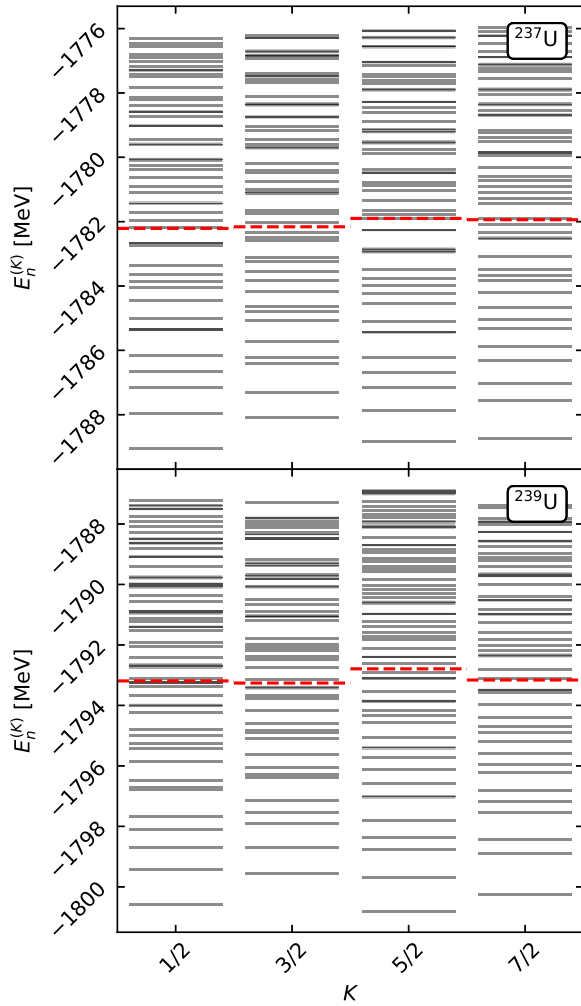
FIG. 7. Spectrum of quasi-bound states for each spin projection K obtained by solving the static GCM+GOA equation within the extrapolated ground-state potential well; see Ref. [52] for details. The red dashed line corresponds to the energy at the saddle point, which defines the barrier.

Gaussian functions of the energy

$$g^{(K)}(\mathbf{q}, t = 0) = \sum_n \exp\left[\frac{\left(E_n^{(K)} - \bar{E}^{(K)}\right)^2}{2\sigma^2}\right] g_n^{(K)}(\mathbf{q}), \quad (33)$$

where $E_n^{(K)}$ is the energy of $g_n^{(K)}$. We show in Fig. 7 the spectra of such quasibound states for ^{237,239}U.

The width σ is a model parameter that controls the spread of the initial collective wave packet. In this work, we set $\sigma = 0.5$ MeV. We determined the level density of quasibound states to be approximately 4 MeV^{-1} at the energy of the barrier and about 7 MeV^{-1} at 5 MeV above the fission barrier. Thus, we have between 20 and 40 quasibound states contributing to the initial state. The parameter $\bar{E}\langle K\rangle$ is adjusted iteratively in order to ensure that the energy of the initial collective wave packet matches the physical energy E_0 of the compound nucleus. It is convenient to write

$$E_0 = E_{\text{bind.}} + E_{\text{x}}, \quad (34)$$

where $E_{\text{bind.}}$ corresponds to the minimum of the saddle point energies over all K,

$$E_{\text{bind.}} = \min_K \left(E_{\text{bind.}}^{(K)}\right), \quad (35)$$

and $E_{\text{x}} = 0, 1, 2, 3, 4, 5$ MeV represents the excitation energy with respect to this minimum saddle configuration.

2. Calculation of the collective flux

We have simulated the large-amplitude collective motion of the fission process all the way to the formation of the fragments with the computer code FELIX [52]. For each PES with spin projection K, the absorption field $\mathbf{A}_{\text{coll.}} \equiv \mathbf{A}_{\text{coll.}}\langle K\rangle$ in Eq. (30) is parametrized by the absorption rate r and width w, which is equivalent to

$$\mathbf{A}_{\text{coll.}}(\mathbf{q}) = \frac{4r}{w^3} x^3(\mathbf{q}), \quad (36)$$

where $x(\mathbf{q})$ is zero if $\mathbf{q}$ corresponds to a nonscissioned configuration, and is equal to the Euclidean distance to the scission line otherwise. We fix the ratio $\frac{4r}{w^3} = 0.04$ MeV. The scission line is defined as an isoline of the expectation value q_{N} of the Gaussian neck operator. In this work, we fixed $q_{\text{N}}^{\text{sciss}} = 6.5$.

We use the collective inertia tensor defined in Sec. II B 2. The zero-point energy correction is extracted from the GCM+GOA width and the inertia tensor through $\varepsilon = \frac{1}{2}\mathbf{\Gamma}\mathbf{M}^{-1}$ in the perturbative cranking approximation of the GCM [3]. The collective wave function $g\langle K\rangle$ is discretized using a rectangular cell mesh with a finite element basis of degree 4, where the nodes are located on the zeros of the Gauss-Lobatto quadrature of order 5. We use a timestep of $\Delta t = 2\times10^{-25}$ s and run the simulation up to $t_{\text{max}} = 3\times10^{-20}$ s.

To determine the yields, we first decompose the scission line $\mathcal{S}$ into small segments ξ. We model the probability $P_{\text{R}}(A, \xi)$ for the right fragment at the segment ξ to have mass A as an integrated Gaussian,

$$P_{\text{R}}(A, \xi) = \int_{A-\frac{1}{2}}^{A+\frac{1}{2}} \frac{\mathrm{d}a}{\sigma_{\text{A}}\sqrt{2\pi}} \exp\left[-\frac{(a - A_{\text{R}}(\xi))^2}{2\sigma_{\text{A}}^2}\right], \quad (37)$$

where $A_{\text{R}}(\xi)$ is the average number of particles in the right fragment and σ_{A} is a parameter of our model that represents the particle-number dispersion in the right fragment and a mass resolution of the experimental data we use to compare with our results. Following earlier studies [45], we use $\sigma_{\text{A}} = 4.0$. We then determine the integrated flux $F(\xi)$ across the element $\xi \in \mathcal{S}$ according to the implementation in [43]. We recall that the integrated flux reads

$$F(\xi) = \lim_{T\to\infty} F(\xi, T) \quad (38)$$

with

$$F(\xi, T) = \int_0^T \mathrm{dt} \int_{\mathbf{q}\in\xi} \mathbf{J}(\mathbf{q}, \mathrm{t}) \cdot \mathrm{d}\mathbf{S}. \quad (39)$$

In that expression, $\mathbf{J}(\mathbf{q}, t)$ is the instantaneous flux at a point $\mathbf{q}$ and time t and is determined using

$$\mathbf{J}(\mathbf{q}, t) = \frac{\hbar}{2i}\sqrt{\gamma(\mathbf{q})}B(\mathbf{q})[g^*(\mathbf{q}, t)\nabla g(\mathbf{q}, t) - g(\mathbf{q}, t)\nabla g^*(\mathbf{q}, t)]. \quad (40)$$

TABLE II. Values of $C_{\text{flux}}(T \to \infty)$ for the two reactions $^{236,238}\mathrm{U}(n, f)$. All values are given in percent.

Target	K	E_x [MeV]					
		0	1	2	3	4	5
$^{236}\mathrm{U}$	1/2	23.9	27.4	25.9	26.0	26.2	25.1
	3/2	23.9	24.2	23.0	23.5	22.9	22.5
	5/2	18.1	20.2	16.2	14.2	12.4	13.8
	7/2	15.7	13.5	14.3	16.6	19.5	18.3
$^{238}\mathrm{U}$	1/2	21.5	25.0	22.9	21.8	20.3	20.9
	3/2	17.9	19.0	19.5	19.0	18.5	20.8
	5/2	9.3	8.5	10.2	10.4	13.6	13.6
	7/2	21.2	21.8	23.3	23.5	24.3	23.7

Finally, we can determine the primary fission fragment mass distributions $Y(A)$ through

$$Y(A) = \sum_{\xi \in \mathcal{S}} F(\xi) \, P_{\mathrm{R}}(A, \xi) \,. \tag{41}$$

Finally, we noticed that the determination of the fission fragments by integration of the flux across the scission line could include spurious negative contributions caused by a part of the wave packet going back through the scission line from the opposite direction. We quantify this effect using

$$C_{\text{flux}}(T) = \frac{\int_0^T dt \int_{\mathcal{S}} d\xi \, \max(-F(\xi, t), 0)}{\int_0^T dt \int_{\mathcal{S}} d\xi \, |F(\xi, t)|} \,. \tag{42}$$

The results for the reactions $^{236,238}\mathrm{U}(n, f)$ are collected in Table II for the scission configurations defined by the condition $q_{\mathrm{N}}^{\text{sciss}} = 6.5$. We find a value around 25%. However, an important proportion of it probably comes from tiny oscillations around the scission line, which would not drastically impact the fission fragment mass distributions. Although a more in-depth analysis of this effect is needed, we use this criteria as an upper bound for the error.

We must also associate the different values of E_x with the energy of an incoming neutron in order to be able to compare our results with experimental data. For fissionable isotopes, fission only occurs when the incident neutron energy is higher than some threshold $E_{\mathrm{n}}^{\mathrm{f}}$. Measurements suggest $E_{\mathrm{n}}^{\mathrm{f}} \approx 0.7$ MeV for the $^{236}\mathrm{U}(n, f)$ reaction [94] while $E_{\mathrm{n}}^{\mathrm{f}} \approx 1.2$ MeV for the $^{238}\mathrm{U}(n, f)$ reaction [94,95]. In such cases, we can assume that our results at $E_x = 0$ should be compared with $E_{\mathrm{n}} = E_{\mathrm{n}}^{\mathrm{f}}$, and this leads to the simple generalization at higher incident energies: $E_{\mathrm{n}} = E_{\mathrm{n}}^{\mathrm{f}} + E_x$. One of the limitations in this work is that we assume axial symmetry: as mentioned in the introduction to this section, fission barriers are therefore systematically overestimated. We account for this effect by assuming a generic offset $\Delta E_{\text{triax.}} = 1$ MeV. This leads to the approximate conversion between incident neutron energy and collective energy,

$$E_{\mathrm{n}} = E_{\mathrm{n}}^{\mathrm{f}} + \Delta E_{\text{triax.}} + E_x. \tag{43}$$

Note that Eq. (43) implicitly depends on the neutron separation energy of the target. Indeed, for a fission reaction with an
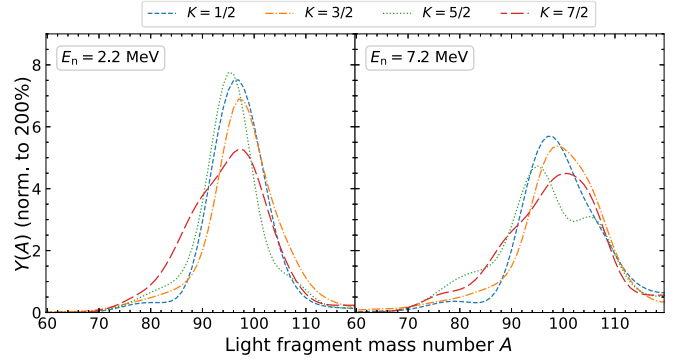

FIG. 8. The first four K components of the mass distribution of the light fission fragment in the $^{238}\mathrm{U}(n, f)$ reaction, before prompt emission, at incident neutron energy $E_{\mathrm{n}} = 2.2$ MeV (left) and $E_{\mathrm{n}} = 7.2$ MeV (right). Each curve has been independently normalized to 200%.

energy threshold $E_{\mathrm{n}}^{\mathrm{f}}$ such as $^{237}\mathrm{U}(n, f)$, we must have $S(N) + E_{\mathrm{n}}^{\mathrm{f}} = E_{\mathrm{A}}$, where E_{A} is the fission barrier height. Hence, $E_{\mathrm{n}}^{\mathrm{f}} = S(N) - E_{\mathrm{A}}$ in this case. However, we can also write the total energy of the fissioning system as $E = E_{\mathrm{g.s.}} + E_{\mathrm{A}} + E_x = E_{\mathrm{g.s.}} + S(N) + E_{\mathrm{n}}^{\mathrm{f}} + E_x$ as well as $E = E_{\mathrm{g.s.}} + S(N) + E_{\mathrm{n}}$. Thus, equating the right-hand side of both definitions, we can simplify by $E_{\mathrm{g.s.}} + S(N)$ which removes the dependency in $E_{\mathrm{g.s.}}$ and $S(N)$ in the relation between E_{n} and $E_{\mathrm{n}}^{\mathrm{f}}$. In contrast, reactions such as $^{235}\mathrm{U}(n, f)$ and $^{237}\mathrm{U}(n, f)$ fission already occurs for thermal neutrons [96,97], hence the threshold for fission is $E_{\mathrm{n}}^{\mathrm{f}} = 0$ MeV. It means that $S(N) > E_{\mathrm{A}}$, and thus we cannot use $S(N)$ in the same way to relate the neutron energy E_{n} with the excitation energy E_x. Instead, we can write that the energy of the fissioning system after neutron absorption is $E = E_{\mathrm{g.s.}} + S(N) + E_{\mathrm{n}} = E_{\mathrm{g.s.}} + E_{\mathrm{A}} + E_x$. Thus, we get $E_{\mathrm{n}} = E_{\mathrm{A}} + E_x - S(N)$.

3. Analysis of $^{238}\mathrm{U}(n, f)$

In this section, we focus on the case of the $^{238}\mathrm{U}(n, f)$ reaction to analyze the impact of the prescription outlined in the two previous sections on the primary fission fragment distributions. Figure 8 shows the primary mass distributions of the light fragment produced in the fission of $^{239}\mathrm{U}$ for different spin projections K and at two different incident neutron energies. The differences between the curves for each K value are meaningful since all the ingredients in the calculation (definition of the scission configurations, characteristics of the TDGCM+GOA, post-processing of the collective flux, etc.) are identical in all four cases: the only differences are the values of the potential energy and collective inertia tensor. Although Fig. 6 shows the population probability of $K = \frac{1}{2}$ is about twice that of $K = \frac{3}{2}$, the probability of populating states with higher K is not negligible and so the differences in mass distributions are important. As the incident neutron energy increases, the probability to populate states of higher K also increases, further magnifying the importance of considering the contributions of different spin projections.

To study the impact of these specific fission-spin channels on the primary mass distribution $Y(A)$ we look for the

available experimental data. Mass distributions from fission reactions induced by fast neutrons are limited and only available for some standard fission reactions important for nuclear technology. One example is the primary mass distributions of the ^{238}U(n, f) reaction from $E_n^{(\text{exp})} = 1.2$ to 5.8 MeV [98]. The energies of the two fragments after prompt particle emission were measured with a dual Frisch-grid ionization chamber and the primary fragment masses were determined using the double-kinetic energy technique. Provisional masses of the two fragments were estimated based on conservation of momentum and the assumption that the fragments were detected back-to-back. Then, the energy of the primary fragments (before neutron emission) was computed based on the expected number of neutrons emitted by each fragment $\nu(A)$. The provisional masses were updated based on the preneutron energies, and this was repeated until the change in the fragment masses from one iteration to the next was less than some fraction of a mass unit. The authors of Ref. [98] assumed a sawtooth-like shape for $\nu(A)$; however, the shape of the neutron distribution as well as the average total number of emitted neutrons as a function of incident neutron energy have been estimated based on available data from neighboring fissioning systems. Since the number of neutrons emitted by each fragment is unknown, the mass of the fragments in a single event cannot be determined more accurately than 4–5 mass units [full width at half-maximum (FWHM)]. It should also be noted that using this technique the primary mass yields in light and heavy groups are symmetric relative to half of the mass number of the fissioning nucleus ($A = 239$ in this case).

In Fig. 9 we compare our calculation of these primary mass distributions of ^{239}U (for the light fragment) with the available experimental dataset of the ^{238}U(n, f) reaction [98] for several incident neutron energies up to the onset of second-chance fission. The error band was obtained by considering an error of ± 1 MeV in the relation given by Eq. (43). Overall, the comparison is rather satisfactory for a "first-principles" approach to the calculation of the mass distribution, especially since potential energy surfaces in two-dimensional (q_{20}, q_{30}) spaces are known to exhibit several spurious discontinuities [99], the removal of which would require increasing the number of collective variables [100–102]. In addition, it was also shown that, at least in two dimensions, calculations with collective variables based on the expectation value of multipole moments could not map all possible fragmentations [41].

B. Independent yields

As mentioned in Sec. II, the primary fission fragments will be sufficiently excited to evaporate neutrons in less than 10^{-15} s. These very short times mean that in any experiment the nuclei that are detected are not the primary fragments, but instead THE secondary fragments resulting from the emission of a varying number of neutrons. As discussed in the previous section, the "experimental" primary yields presented in Fig. 9 were reconstructed from measurements of independent yields following a model-dependent procedure.
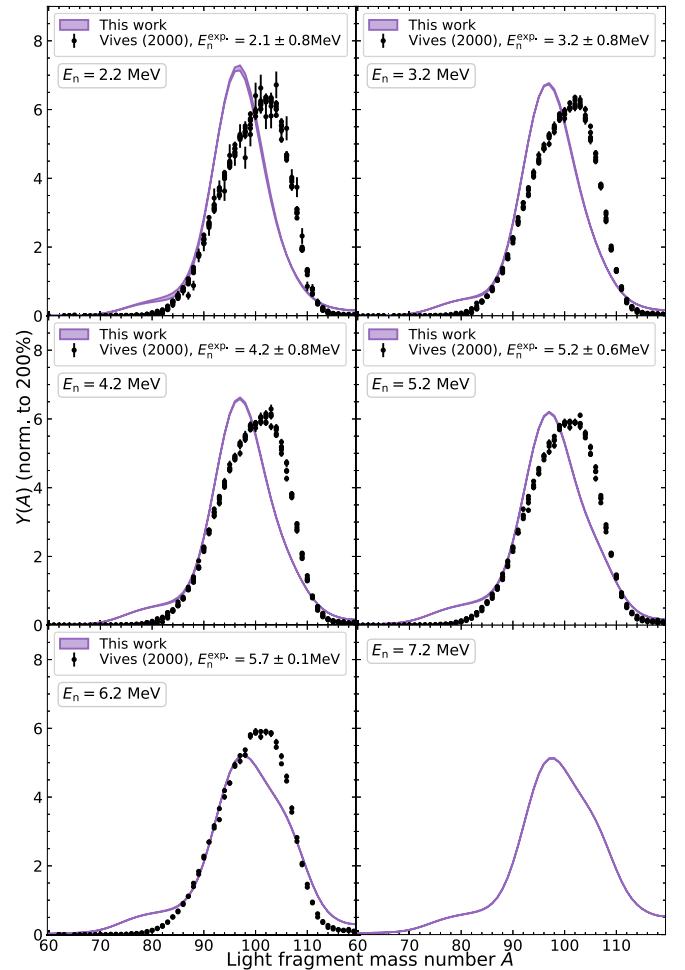

FIG. 9. Mass distribution of the light fission fragment in the ^{238}U(n, f) reaction, before prompt emission, as a function of incident neutron energy. Experimental data are taken from Ref. [98].

However, independent yields can also be computed from the primary ones by simulating the emission of prompt neutrons and photons. As is commonly known, the main drawback of doing so is that one needs to completely characterize the fission fragments at scission: not just their distribution $Y(Z, A)$ but also their excitation energy E^*, spin-parity distribution $p(J^\pi)$, and level density $\rho(E^*, J^\pi)$. In spite of very encouraging progress in recent years, a predictive model of *all* such quantities does not yet exist [1]. Evaluations of fission product yields typically rely on various empirical models with parameters adjusted to data. We adopt a similar strategy here: the prompt emission of particles is simulated with the event generator FREYA [91,92].

By default, FREYA can calculate fission events of the ^{238}U(n, f) reaction; various model parameters have already been adjusted to reproduce experimental data. Therefore, we used the default FREYA setup to process our ^{238}U(n, f) primary yields with only two modifications: (i) we replaced the default five-Gaussian parametrization of the primary mass distribution with our calculated ones at $E_n = 2.2$ MeV; and (ii) we changed the parameter dTKE, which is an overall energy shift to the total kinetic energy. FREYA determines the total kinetic
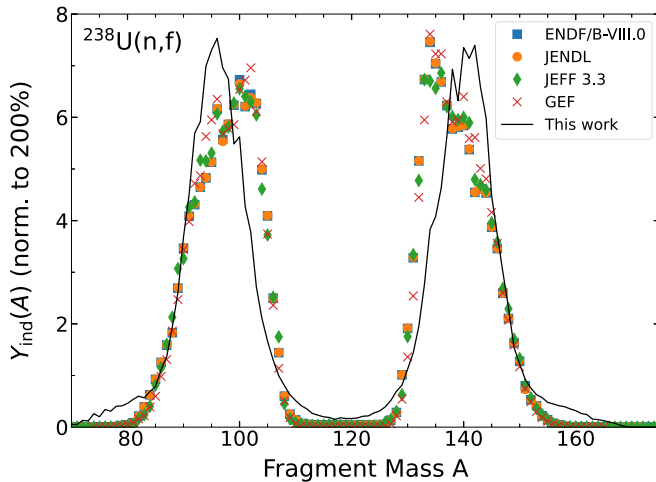
FIG. 10. Fission fragment mass distribution of the ^{238}U(n, f) reaction after neutron emission for an incident neutron energy $E_n = 2.2$ MeV. The present results are compared with a GEF-2021/1.1 [103] empirical model calculation at $E_n = 2.2$ MeV and the following evaluations for fast-neutron-induced fission: ENDF/B-VIII.0 [96], JEFF-3.3 [104], and JENDL-5 [105].

FIG. 11. Fission fragment mass distribution of the ^{236}U(n, f) reaction after neutron emission for an incident neutron energy $E_n = 1.7$ MeV. The present results are compared with a GEF-2021/1.1 [103] empirical model calculation at $E_n = 1.7$ MeV and the following evaluations for fast-neutron-induced fission: ENDF/B-VIII.0 [96], JEFF-3.3 [104], and JENDL-5 [105].

energy for a pair of fragments using experimental data, and the shift dTKE is tuned to reproduce the prompt neutron multiplicity, $\bar{\nu}$. We adjusted dTKE for $E_n = 2.2$ MeV from its default value of 1.0 MeV to 0.698 MeV in order to match the ENDF/B-VIII.0 value $\bar{\nu} = 2.605$.

Figure 10 compares our calculations with several evaluations of the independent mass yields in the reaction ^{238}U(n, f) at an incident neutron energy of $E_n = 2.2$ MeV. The agreement with the data is rather good considering that the primary mass distribution comes from a model prediction rather than an empirical fit. The main limitation is that the distance between the two peaks is slightly too wide. This is most likely caused by the fact that the mass of the heavy fragments is overestimated. We note that symmetric and very asymmetric fission are also overestimated.

FREYA has not been tuned for the ^{236}U(n, f) reaction, so we added that reaction and generally kept the default values of any of the model parameters. As for the case of ^{238}U(n, f), we replaced the default primary mass yields with our calculated fission fragment mass distribution, this time at $E_n = 1.7$ MeV. Pre-equilibrium neutron emission was disabled since there is no available data for this process for this reaction. There is also no suitable experimental database or evaluation for the total kinetic energy as a function of fragment mass for the ^{236}U(n, f) reaction. For this reason, we took the experimental data from the ^{235}U(n, f) reaction instead. The parameter dTKE was set to -1.480 MeV to reproduce the ENDF/B-VIII.0 value $\bar{\nu} = 2.545$ for $E_n = 1.7$ MeV.

As shown in Fig. 11, results for ^{236}U(n, f) are somewhat similar to ^{238}U(n, f). Again, both symmetric and very asymmetric fission are overestimated. This time, however, the centroids of the light and heavy mass peaks are much closer to the evaluated values. The yields we compute are slightly lower than the evaluated one, especially in the heavy peak. This may be caused by the fact that our scission configurations
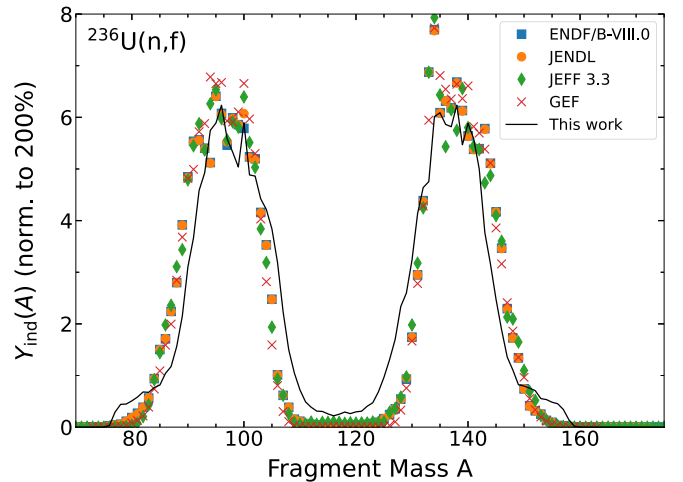
near the most likely fission lack some fragmentations around $A_H \approx 135$. This problem is reminiscent of issues identified earlier in potential energy surfaces obtained with constraints on standard multipole moments [41,106].

V. CONCLUSIONS

In this work, we established a rigorous procedure to compute the fission fragment mass distributions before the emission of prompt neutrons within the general framework of nuclear energy density functional theory. Our method assumes that the nuclear shape is axially symmetric and requires three ingredients: (i) the spin distribution of the fissioning nucleus, which we obtain from the coupled-channel formalism; (ii) the potential energy surfaces for different spin projections K, which are computed within the Hartree-Fock-Bogoliubov theory with the equal filling approximation of the blocking prescription; and (iii) the collective inertia tensor determined by the finite-temperature extension of the adiabatic time-dependent Hartree-Fock-Bogoliubov theory. For the latter, we sketched the complete derivation of the formulas used without proof so far in the literature.

We tested our approach on the ^{236}U(n, f) and ^{238}U(n, f) fission reactions, which leads to the odd-mass compound nuclei ^{237}U and ^{239}U, respectively. We confirmed that the choice of the blocking configuration has a major impact on deformation properties: fission barrier heights, which are key ingredients in the evaluation of fission cross sections and probabilities, can vary by up to 1–2 MeV depending on the choice of blocked quasiparticle [21]. We also showed that the fission fragment distributions obtained for different K configurations are significantly dissimilar and that the different population probabilities of each spin channel can magnify these differences. We emphasized that mapping the collective

wave packet's energy with the incident neutron's kinetic energy is much more challenging in odd-mass systems since each spin channel has a different barrier height. We simulated the prompt emission of particles with the code FREYA to compare our calculations with experimental data. Overall, the agreement between our model and experimental data is satisfactory.

Combining our microscopic approach of computing primary fission observables with the fission simulation model FREYA opens up the possibility to study the impact of different entrance channels on fission-fragment mass distributions. A systematic comparison of fission-product yields emerging from different angular momenta transfer to the compound system is now potentially feasible. We have also provided a framework for large-scale fission calculations of odd-mass nuclei involved, e.g., in *r*-process nucleosynthesis, for which no experimental data exists. As often in self-consistent calculations, our two-dimensional potential energy surfaces are plagued by several discontinuities. To turn our theoretical framework into a competitive evaluation tool, one must enlarge the collective space and develop algorithms capable of eliminating spurious discontinuities. Only then will a proper quantification of theoretical uncertainties associated with, e.g., the definition of scission configurations or the choice of

the inertia tensor or zero-point energy contributions, will truly make sense.

In the particular case of odd-mass nuclei, it could be worthwhile to study the impact of the blocking approximation itself, especially as it pertains to the collective inertia tensor. In this work, we used the cranking approximation in its perturbative version, where the quasiparticle random phase approximation (QRPA) matrix is diagonal and all derivatives are computed locally. The analysis of Ref. [107] showed considerable differences between such a cranking approximation and the "exact" calculation. Since solving the QRPA involves the time-odd channel of the functional, this suggests that there could be a sizable effect of time-reversal-symmetry breaking in the collective inertia tensor—hence in the collective dynamics—which might be further magnified in odd-mass systems.

ACKNOWLEDGMENTS

[1] N. Schunck and D. Regnier, Theory of nuclear fission, Prog. Part. Nucl. Phys. **125**, 103963 (2022).

[2] M. Bender, R. Bernard, G. Bertsch, S. Chiba, J. Dobaczewski, N. Dubray, S. A. Giuliani, K. Hagino, D. Lacroix, Z. Li, P. Magierski, J. Maruhn, W. Nazarewicz, J. Pei, S. Péru, N. Pillet, J. Randrup, D. Regnier, P.-G. Reinhard, L. M. Robledo, W. Ryssens, J. Sadhukhan, G. Scamps, N. Schunck, C. Simenel, J. Skalski, I. Stetcu, P. Stevenson, S. Umar, M. Verriere, D. Vretenar, M. Warda, and S. Åberg, Future of nuclear fission theory, J. Phys. G: Nucl. Part. Phys. **47**, 113002 (2020).

[3] N. Schunck and L. M. Robledo, Microscopic theory of nuclear fission: A review, Rep. Prog. Phys. **79**, 116301 (2016).

[4] G. Scamps and C. Simenel, Impact of pear-shaped fission fragments on mass-asymmetric fission in actinides, Nature (London) **564**, 382 (2018).

[5] G. Scamps, C. Simenel, and D. Lacroix, Superfluid dynamics of ^{258}Fm fission, Phys. Rev. C **92**, 011602(R) (2015).

[6] Y. Tanimura, D. Lacroix, and G. Scamps, Collective aspects deduced from time-dependent microscopic mean-field with pairing: Application to the fission process, Phys. Rev. C **92**, 034601 (2015).

[7] A. Bulgac, P. Magierski, K. J. Roche, and I. Stetcu, Induced Fission of ^{240}Pu within a Real-Time Microscopic Framework, Phys. Rev. Lett. **116**, 122504 (2016).

[8] A. Bulgac, S. Jin, K. J. Roche, N. Schunck, and I. Stetcu, Fission dynamics of ^{240}Pu from saddle to scission and beyond, Phys. Rev. C **100**, 034615 (2019).

[9] A. Bulgac, I. Abdurrahman, S. Jin, K. Godbey, N. Schunck, and I. Stetcu, Fission Fragment Intrinsic Spins and Their Correlations, Phys. Rev. Lett. **126**, 142502 (2021).

[10] P. Marević, N. Schunck, J. Randrup, and R. Vogt, Angular momentum of fission fragments from microscopic theory, Phys. Rev. C **104**, L021601 (2021).

[11] A. Bulgac, I. Abdurrahman, K. Godbey, and I. Stetcu, Fragment Intrinsic Spins and Fragments' Relative Orbital Angular Momentum in Nuclear Fission, Phys. Rev. Lett. **128**, 022501 (2022).

[12] G. Martínez-Pinedo, D. Mocelj, N. Zinner, A. Kelić, K. Langanke, I. Panov, B. Pfeiffer, T. Rauscher, K.-H. Schmidt, and F.-K. Thielemann, The role of fission in the r-process, Prog. Part. Nucl. Phys. **59**, 199 (2007).

[13] F. K. Thielemann, A. Arcones, R. Käppeli, M. Liebendörfer, T. Rauscher, C. Winteler, C. Fröhlich, I. Dillmann, T. Fischer, G. Martinez-Pinedo, K. Langanke, K. Farouqi, K.-L. Kratz, I. Panov, and I. K. Korneev, What are the astrophysical sites for the r-process and the production of heavy elements?, Prog. Part. Nucl. Phys. **66**, 346 (2011).

[14] M. R. Mumpower, R. Surman, G. C. McLaughlin, and A. Aprahamian, The impact of individual nuclear properties on r-process nucleosynthesis, Prog. Part. Nucl. Phys. **86**, 86 (2016).

[15] A. A. Sonzogni, E. A. McCutchan, and A. C. Hayes, Dissecting Reactor Antineutrino Flux Calculations, Phys. Rev. Lett. **119**, 112501 (2017).

[16] K. H. Schmidt, M. Estienne, M. Fallot, S. Cormon, A. Cucoanes, T. Shiba, B. Jurado, K. Kern, and C. Schmitt, Extensive study of the quality of fission yields from experiment, evaluation and GEF for antineutrino studies and applications, Nucl. Data Sheets Special Issue Nucl. React. Data **173**, 54 (2021).

[17] A. E. Lovell, T. Kawano, S. Okumura, I. Stetcu, M. R. Mumpower, and P. Talou, Extension of the Hauser-Feshbach fission fragment decay model to multichance fission, Phys. Rev. C **103**, 014615 (2021).

[18] T. Kawano, S. Okumura, A. E. Lovell, I. Stetcu, and P. Talou, Influence of nonstatistical properties in nuclear structure on

emission of prompt fission neutrons, Phys. Rev. C **104**, 014611 (2021).

[19] P. Talou, I. Stetcu, P. Jaffke, M. E. Rising, A. E. Lovell, and T. Kawano, Fission fragment decay simulations with the CGMF code, Comput. Phys. Commun. **269**, 108087 (2021).

[20] K. M. Hock, L. Bonneau, P. Quentin, and H. Wagiran, Fission barriers of odd-mass nuclei within the HF-BCS and HTDA approaches, EPJ Web Conf. **62**, 04004 (2013)

[21] M.-H. Koh, L. Bonneau, P. Quentin, T. V. Nhan Hao, and H. Wagiran, Fission barriers of two odd-neutron actinide nuclei taking into account the time-reversal symmetry breaking at the mean-field level, Phys. Rev. C **95**, 014315 (2017).

[22] S. Perez-Martin and L. M. Robledo, Fission properties of odd-A nuclei in a mean field framework, Int. J. Mod. Phys. E **18**, 788 (2009).

[23] R. Rodríguez-Guzmán and L. M. Robledo, Microscopic description of fission in odd-mass uranium and plutonium nuclei with the Gogny energy density functional, Eur. Phys. J. A **53**, 245 (2017).

[24] N. Schunck, *Energy Density Functional Methods for Atomic Nuclei*, IOP Expanding Physics (IOP Publishing, Bristol, UK, 2019).

[25] R. W. Mills, Fission product yield evaluation, Ph.D. thesis, University of Birmingham (1995).

[26] C. Wagemans, *The Nuclear Fission Process* (CRC Press, Boca Raton, FL, 1991).

[27] H. Feshbach, A. Kerman, and S. Koonin, The statistical theory of multi-step compound and direct reactions, Ann. Phys. (NY) **125**, 429 (1980).

[28] A. J. Koning, S. Hilaire, and M. C. Duijvestijn, TALYS-1.0, in *Proceedings of theerence on Nuclear Data Science Technologies* (EDP Sciences, Nice, France, 2008), p. 211.

[29] M. Herman, R. Capote, B. V. Carlson, P. Obložinský, M. Sin, A. Trkov, H. Wienke, and V. Zerkin, EMPIRE: Nuclear reaction model code system for data evaluation, Nucl. Data Sheets Special Issue Evaluat. Neut. Cross Sect. **108**, 2655 (2007).

[30] T. Kawano, P. Talou, M. B. Chadwick, and T. Watanabe, Monte Carlo simulation for particle and γ-ray emissions in statistical Hauser-Feshbach model, J. Nucl. Sci. Technol. **47**, 462 (2010).

[31] W. Ormand, Monte Carlo Hauser-Feshbach Computer Code System to Model Nuclear Reactions: YAHFC, Technical Report No. LLNL-TR-824700, 1808762, 1038262, Lawrence Livermore National Laboratory (LLNL), Livermore, CA, 2021.

[32] A. Bohr and B. R. Mottelson, *Nuclear Structure*, Vol. II (Benjamin, New York, 1975).

[33] T. Tamura, Analyses of the scattering of nuclear particles by collective nuclei in terms of the coupled-channel calculation, Rev. Mod. Phys. **37**, 679 (1965).

[34] E. S. Soukhovitskiĭ, R. Capote, J. M. Quesada, S. Chiba, and D. S. Martyanov, Nucleon scattering on actinides using a dispersive optical model with extended couplings, Phys. Rev. C **94**, 064605 (2016).

[35] M. Verriere and D. Regnier, The time-dependent generator coordinate method in nuclear physics, Front. Phys. **8**, 233 (2020).

[36] J. F. Berger, M. Girod, and D. Gogny, Microscopic analysis of collective dynamics in low energy fission, Nucl. Phys. A **428**, 23 (1984).

[37] J. F. Berger, Quantum dynamics of wavepackets on two-dimensional potential energy surfaces governing nuclear fission, in *Dynamics of Wave Packets in Molecular and Nuclear Physics*, edited by J. Broeckhove, L. Lathouwers, and P. van Leuven, Lecture Notes in Physics No. 256 (Springer, Berlin/Heidelberg, 1986), p. 21.

[38] J. F. Berger, M. Girod, and D. Gogny, Time-dependent quantum collective dynamics applied to nuclear fission, Comput. Phys. Commun. **63**, 365 (1991).

[39] H. Goutte, P. Casoli, and J.-F. Berger, Mass and kinetic energy distributions of fission fragments using the time dependent generator coordinate method, Nucl. Phys. A **734**, 217 (2004).

[40] H. Goutte, J.-F. Berger, P. Casoli, and D. Gogny, Microscopic approach of fission dynamics applied to fragment kinetic energy and mass distributions in ^{238}U, Phys. Rev. C **71**, 024316 (2005).

[41] W. Younes and D. Gogny, Fragment Yields Calculated in a Time-Dependent Microscopic Theory of Fission, Technical Report No. LLNL-TR-586678, Lawrence Livermore National Laboratory (LLNL), Livermore, CA, 2012.

[42] D. Regnier, N. Dubray, N. Schunck, and M. Verrière, Fission fragment charge and mass distributions in ^{239}Pu(n,f) in the adiabatic nuclear energy density functional theory, Phys. Rev. C **93**, 054611 (2016).

[43] D. Regnier, M. Verrière, N. Dubray, and N. Schunck, FELIX-1.0: A finite element solver for the time dependent generator coordinate method with the Gaussian overlap approximation, Comput. Phys. Commun. **200**, 350 (2016).

[44] W. Younes, D. Marc Gogny, and J.-F. Berger, *A Microscopic Theory of Fission Dynamics Based on the Generator Coordinate Method*, Lectures Notes in Physics, Vol. 950 (Springer International Publishing, Berlin, 2019).

[45] M. Verriere, N. Schunck, and D. Regnier, Microscopic calculation of fission product yields with particle-number projection, Phys. Rev. C **103**, 054602 (2021).

[46] H.-J. Mang, The self-consistent single-particle model in nuclear physics, Phys. Rep. **18**, 325 (1975).

[47] A. Faessler, M. Ploszajczak, and K. W. Schmid, Description of high spin states, Prog. Part. Nucl. Phys. **5**, 79 (1981).

[48] T. Duguet, P. Bonche, P.-H. Heenen, and J. Meyer, Pairing correlations. I. Description of odd nuclei in mean-field theories, Phys. Rev. C **65**, 014310 (2001).

[49] N. Schunck, J. Dobaczewski, J. McDonnell, J. Moré, W. Nazarewicz, J. Sarich, and M. V. Stoitsov, One-quasiparticle states in the nuclear energy density functional theory, Phys. Rev. C **81**, 024316 (2010).

[50] S. Perez-Martin and L. M. Robledo, Microscopic justification of the equal filling approximation, Phys. Rev. C **78**, 014304 (2008).

[51] M. Stoitsov, N. Schunck, M. Kortelainen, N. Michel, H. Nam, E. Olsen, J. Sarich, and S. Wild, Axially deformed solution of the Skyrme-Hartree-Fock-Bogoliubov equations using the transformed harmonic oscillator basis (II) HFBTHO v2.00d: A new version of the program, Comput. Phys. Commun. **184**, 1592 (2013).

[52] D. Regnier, N. Dubray, M. Verrière, and N. Schunck, FELIX-2.0: New version of the finite element solver for the time dependent generator coordinate method with the Gaussian overlap approximation, Comput. Phys. Commun. **225**, 180 (2018).

[53] H. Krappe and K. Pomorski, *Theory of Nuclear Fission* (Springer, Berlin, 2012).

[54] V. Martin and L. M. Robledo, Fission barriers at finite temperature: A theoretical description with the Gogny force, Int. J. Mod. Phys. E **18**, 861 (2009).

[55] Y. Zhu and J. C. Pei, Thermal fission rates with temperature dependent fission barriers, Phys. Rev. C **94**, 024329 (2016).

[56] J. Zhao, T. Nikšić, D. Vretenar, and S.-G. Zhou, Microscopic self-consistent description of induced fission dynamics: Finite-temperature effects, Phys. Rev. C **99**, 014618 (2019).

[57] J. Zhao, T. Nikšić, and D. Vretenar, Time-dependent generator coordinate method study of fission: Dissipation effects, Phys. Rev. C **105**, 054604 (2022).

[58] A. Iwamoto and J. A. Maruhn, The behavior of the temperature-dependent cranking mass parameter, Z. Phys. A **293**, 315 (1979).

[59] A. Baran and Z. Lojewski, Temperature dependence of mass parameters and fission barriers, Acta Phys. Pol. B **25**, 1231 (1994).

[60] H. M. Sommermann, Microscopic description of giant resonances in highly excited nuclei, Ann. Phys. (NY) **151**, 163 (1983).

[61] J.-P. Blaizot and G. Ripka, *Quantum Theory of Finite Systems* (MIT Press, Cambridge, 1985).

[62] M. Baranger and M. Veneroni, An adiabatic time-dependent Hartree-Fock theory of collective motion in finite systems, Ann. Phys. (NY) **114**, 123 (1978).

[63] S. E. Larsson, I. Ragnarsson, and S. G. Nilsson, Fission barriers and the inclusion of axial asymmetry, Phys. Lett. B **38**, 269 (1972).

[64] T. Bürvenich, M. Bender, J. A. Maruhn, and P.-G. Reinhard, Systematics of fission barriers in superheavy elements, Phys. Rev. C **69**, 014307 (2004).

[65] M. Kowal, P. Jachimowicz, and A. Sobiczewski, Fission barriers for even-even superheavy nuclei, Phys. Rev. C **82**, 014303 (2010).

[66] H. Abusara, A. V. Afanasjev, and P. Ring, Fission barriers in actinides in covariant density functional theory: The role of triaxiality, Phys. Rev. C **82**, 044303 (2010).

[67] B.-N. Lu, E.-G. Zhao, and S.-G. Zhou, Potential energy surfaces of actinide nuclei from a multidimensional constrained covariant density functional theory: Barrier heights and saddle point shapes, Phys. Rev. C **85**, 011301(R) (2012).

[68] H. Abusara, A. V. Afanasjev, and P. Ring, Fission barriers in covariant density functional theory: Extrapolation to superheavy nuclei, Phys. Rev. C **85**, 024314 (2012).

[69] N. Schunck, D. Duke, H. Carr, and A. Knoll, Description of induced nuclear fission with Skyrme energy functionals: Static potential energy surfaces and fission fragment properties, Phys. Rev. C **90**, 054305 (2014).

[70] P. Marević, N. Schunck, E. M. Ney, R. Navarro Pérez, M. Verriere, and J. O'Neal, Axially-deformed solution of the Skyrme-Hartree-Fock-Bogoliubov equations using the transformed harmonic oscillator basis (IV) HFBTHO (v4.0): A new version of the program, Comput. Phys. Commun. **276**, 108367 (2022).

[71] J. Bartel, P. Quentin, M. Brack, C. Guet, and H.-B. Håkansson, Towards a better parametrisation of Skyrme-like effective forces: A critical study of the SkM force, Nucl. Phys. A **386**, 79 (1982).

[72] S. G. Nilsson, G. Ohlén, C. Gustafson, and P. Möller, On a new type of fission-isometric state, Phys. Lett. B **30**, 437 (1969).

[73] J. Randrup, C. F. Tsang, P. Möller, S. G. Nilsson, and S. E. Larsson, Theoretical predictions of fission half-lives of elements with Z between 92 and 106, Nucl. Phys. A **217**, 221 (1973).

[74] S. Čwiok, Z. Lojewski, and V. V. Pashkevich, Fission barriers of odd-mass nuclei and odd nuclei with $100 \leqslant Z \leqslant 111$, Nucl. Phys. A **444**, 1 (1985).

[75] P. Jachimowicz, M. Kowal, and J. Skalski, Adiabatic fission barriers in superheavy nuclei, Phys. Rev. C **95**, 014303 (2017).

[76] National Nuclear Data Center, https://www.nndc.bnl.gov/ (2019).

[77] W. Younes and W. Loveland, *An Introduction to Nuclear Fission* (Springer, Berlin, 2021).

[78] M. G. Mustafa and K. Kumar, Angular momentum dependence of moments of inertia and fission barriers of 240Pu, Phys. Lett. B **49**, 405 (1974).

[79] M. Diebel, K. Albrecht, and R. W. Hasse, Microscopic calculations of fission barriers and critical angular momenta for excited heavy nuclear systems, Nucl. Phys. A **355**, 66 (1981).

[80] J. Nemeth, D. Dalili, and C. Ngô, Hartree-Fock and Thomas-Fermi self-consistent calculations of the ^{144}Nd nucleus at finite temperature and angular momentum, Phys. Lett. B **154**, 11 (1985).

[81] F. Garcias, M. Barranco, A. Faessler, and N. Ohtsuka, Angular momentum and temperature dependence of fission barriers with a realistic force, Z. Phys. A **336**, 31 (1990).

[82] J. L. Egido and L. M. Robledo, Fission Barriers at High Angular Momentum and the Ground State Rotational Band of the Nucleus ^{254}No, Phys. Rev. Lett. **85**, 1198 (2000).

[83] A. Baran and A. Staszczak, Fission of rotating fermium isotopes, Phys. Scr. **89**, 054002 (2014).

[84] N. Dubray, H. Goutte, and J.-P. Delaroche, Structure properties of ^{226}Th and ^{256,258,260}Fm fission fragments: Mean-field analysis with the Gogny force, Phys. Rev. C **77**, 014310 (2008).

[85] W. Younes and D. Gogny, Microscopic calculation of ^{240}Pu scission with a finite-range effective force, Phys. Rev. C **80**, 054313 (2009).

[86] J. Zhao, B.-N. Lu, D. Vretenar, E.-G. Zhao, and S.-G. Zhou, Multidimensionally constrained relativistic mean-field study of triple-humped barriers in actinides, Phys. Rev. C **91**, 014321 (2015).

[87] H. Tao, J. Zhao, Z. P. Li, T. Nikšić, and D. Vretenar, Microscopic study of induced fission dynamics of ^{226}Th with covariant energy density functionals, Phys. Rev. C **96**, 024319 (2017).

[88] J. Zhao, J. Xiang, Z.-P. Li, T. Nikšić, D. Vretenar, and S.-G. Zhou, Time-dependent generator-coordinate-method study of mass-asymmetric fission of actinides, Phys. Rev. C **99**, 054613 (2019).

[89] A. C. Wahl, Nuclear-charge distribution and delayed-neutron yields for thermal-neutron-induced fission of ^{235}U, ^{233}U, and ^{239}Pu and for spontaneous fission of ^{252}Cf, At. Data Nucl. Data Tables **39**, 1 (1988).

[90] W. Younes and D. Gogny, Nuclear Scission and Quantum Localization, Phys. Rev. Lett. **107**, 132501 (2011).

[91] J. M. Verbeke, J. Randrup, and R. Vogt, Fission Reaction Event Yield Algorithm, FREYA–For event-by-event simulation of fission, Comput. Phys. Commun. **191**, 178 (2015).

[92] J. M. Verbeke, J. Randrup, and R. Vogt, Fission reaction event yield algorithm FREYA 2.0.2, Comput. Phys. Commun. **222**, 263 (2018).

[93] I. J. Thompson, Coupled reaction channels calculations in nuclear physics, Comput. Phys. Rep. **7**, 167 (1988).

[94] F. Tovesson, A. Laptev, and T. S. Hill, Fast neutron–induced fission cross sections of ^{233,234,236,238}U up to 200 MeV, Nucl. Sci. Eng. **178**, 57 (2014).

[95] O. Shcherbakov, A. Donets, A. Evdokimov, A. Fomichev, T. Fukahori, A. Hasegawa, A. Laptev, V. Maslov, G. Petrov, S. Soloviev, Y. Tuboltsev, and A. Vorobyev, Neutron-induced fission of ^{233}U, ^{238}U, ^{232}Th, ^{239}Pu, ^{237}Np, ^{nat}Pb and ^{209}Bi relative to ^{235}U in the energy range 1-200 MeV, J. Nucl. Sci. Technol. **39**, 230 (2002).

[96] D. A. Brown, M. B. Chadwick, R. Capote, A. C. Kahler, A. Trkov, M. W. Herman, A. A. Sonzogni, Y. Danon, A. D. Carlson, M. Dunn, D. L. Smith, G. M. Hale, G. Arbanas, R. Arcilla, C. R. Bates, B. Beck, B. Becker, F. Brown, R. J. Casperson, J. Conlin, D. E. Cullen, M.-A. Descalle, R. Firestone, T. Gaines, K. H. Guber, A. I. Hawari, J. Holmes, T. D. Johnson, T. Kawano, B. C. Kiedrowski, A. J. Koning, S. Kopecky, L. Leal, J. P. Lestone, C. Lubitz, J. I. Márquez Damián, C. M. Mattoon, E. A. McCutchan, S. Mughabghab, P. Navratil, D. Neudecker, G. P. A. Nobre, G. Noguere, M. Paris, M. T. Pigni, A. J. Plompen, B. Pritychenko, V. G. Pronyaev, D. Roubtsov, D. Rochman, P. Romano, P. Schillebeeckx, S. Simakov, M. Sin, I. Sirakov, B. Sleaford, V. Sobes, E. S. Soukhovitskii, I. Stetcu, P. Talou, I. Thompson, S. van der Marck, L. Welser-Sherrill, D. Wiarda, M. White, J. L. Wormald, R. Q. Wright, M. Zerkle, G. Žerovnik, and Y. Zhu, ENDF/B-VIII.0: The 8th major release of the nuclear reaction data library with CIELO-project cross sections, new standards and thermal scattering data, Nucl. Data Sheets Special Issue Nucl. React. Data **148**, 1 (2018).

[97] J. H. McNally, J. W. Barnes, B. J. Dropesky, P. A. Seeger, and K. Wolfsberg, Neutron-induced fission cross section of ^{237}U, Phys. Rev. C **9**, 717 (1974).

[98] F. Vivès, F. J. Hambsch, H. Bax, and S. Oberstedt, Investigation of the fission fragment properties of the reaction 238U(n,f) at incident neutron energies up to 5.8 MeV, Nucl. Phys. A **662**, 63 (2000).

[99] N. Dubray and D. Regnier, Numerical search of discontinuities in self-consistent potential energy surfaces, Comput. Phys. Commun. **183**, 2035 (2012).

[100] A. Zdeb, M. Warda, and L. M. Robledo, Description of the multidimensional potential-energy surface in fission of ^{252}Cf and ^{258}No, Phys. Rev. C **104**, 014610 (2021).

[101] R. Han, M. Warda, A. Zdeb, and L. M. Robledo, Scission configuration in self-consistent calculations with neck constraints, Phys. Rev. C **104**, 064602 (2021).

[102] N. W. T. Lau, R. N. Bernard, and C. Simenel, Smoothing of one- and two-dimensional discontinuities in potential energy surfaces, Phys. Rev. C **105**, 034617 (2022).

[103] K.-H. Schmidt, B. Jurado, C. Amouroux, and C. Schmitt, General description of fission observables: GEF model code, Nucl. Data Sheets **131**, 107 (2016).

[104] A. J. M. Plompen, O. Cabellos, C. De Saint Jean, M. Fleming, A. Algora, M. Angelone, P. Archier, E. Bauge, O. Bersillon, A. Blokhin, F. Cantargi, A. Chebboubi, C. Diez, H. Duarte, E. Dupont, J. Dyrda, B. Erasmus, L. Fiorito, U. Fischer, D. Flammini, D. Foligno, M. R. Gilbert, J. R. Granada, W. Haeck, F. J. Hambsch, P. Helgesson, S. Hilaire, I. Hill, M. Hursin, R. Ichou, R. Jacqmin, B. Jansky, C. Jouanne, M. A. Kellett, D. H. Kim, H. I. Kim, I. Kodeli, A. J. Koning, A. Y. Konobeyev, S. Kopecky, B. Kos, A. Krása, L. C. Leal, N. Leclaire, P. Leconte, Y. O. Lee, H. Leeb, O. Litaize, M. Majerle, J. I. Márquez Damián, F. Michel-Sendis, R. W. Mills, B. Morillon, G. Noguère, M. Pecchia, S. Pelloni, P. Pereslavtsev, R. J. Perry, D. Rochman, A. Röhrmoser, P. Romain, P. Romojaro, D. Roubtsov, P. Sauvan, P. Schillebeeckx, K. H. Schmidt, O. Serot, S. Simakov, I. Sirakov, H. Sjöstrand, A. Stankovskiy, J. C. Sublet, P. Tamagno, A. Trkov, S. van der Marck, F. Álvarez-Velarde, R. Villari, T. C. Ware, K. Yokoyama, and G. Žerovnik, The joint evaluated fission and fusion nuclear data library, jeff-3.3, Eur. Phys. J. A **56**, 181 (2020).

[105] O. Iwamoto, N. Iwamoto, K. Shibata, A. Ichihara, S. Kunieda, F. Minato, and S. Nakayama, Status of jendl, EPJ Web Conf. **239**, 09002 (2020).

[106] W. Younes, D. Gogny, and N. Schunck, A microscopic theory of low-energy fission: Fragment properties, in *Fission Properties of Neutron-Rich Nuclei* (World Scientific, Sanibel Island, FL, 2013), p. 605.

[107] K. Washiyama, N. Hinohara, and T. Nakatsukasa, Finite-amplitude method for collective inertia in spontaneous fission, Phys. Rev. C **103**, 014306 (2021).